

**Search for charginos and neutralinos in a signature with a Higgs  
boson and an isolated lepton with the ATLAS detector and its  
reinterpretation in the phenomenological MSSM**



DISSERTATION AN DER FAKULTÄT FÜR PHYSIK  
DER  
LUDWIG-MAXIMILIANS-UNIVERSITÄT MÜNCHEN

vorgelegt von  
Eric Schanet  
aus Luxemburg

München, den 7. Mai 2021





















































































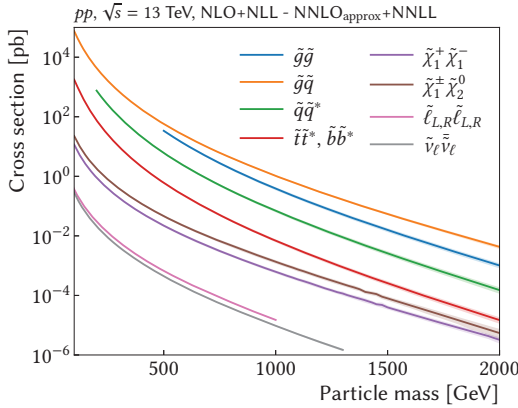


**Figure 1.8:** Cross sections of different SUSY production processes at  $\sqrt{s} = 13$  TeV in  $pp$  collisions. Cross sections for pair production of electroweakinos are significantly smaller than, e.g., those for pair production of gluinos. The shaded bands correspond to the theory uncertainty of each cross section. Cross sections taken for coloured and electroweak sector taken from Refs. [81, 82] and Refs. [83–85], respectively.

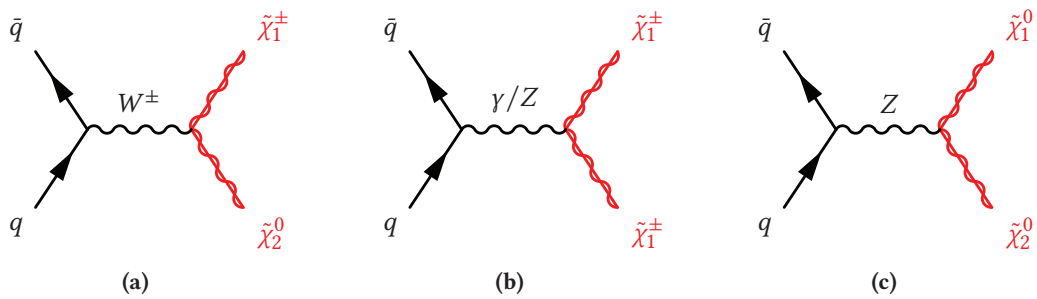


**Figure 1.9:** Dominant diagrams for production of electroweakino pairs at the Large Hadron Collider. Adapted from Ref. [5].

models that include many different production processes and decay modes. Another possibility is to perform reinterpretations of SUSY searches—optimised for one or more such simplified models—in more complete (and high-dimensional) SUSY model spaces, like e.g., in the pMSSM. This cannot only demonstrate the sensitivity of existing SUSY searches beyond simplified models, but also potentially identify blind spots and model regions not covered by current searches. In addition, connections to (in)direct DM searches and various SM measurements can be explored this way. Recent efforts in this direction include, e.g., Refs. [79, 86, 87]. As will be discussed in part III of this thesis, efforts reinterpreting ATLAS searches for SUSY in the pMSSM are currently ongoing. In chapter 11, a reinterpretation of the search for electroweakinos presented herein using a set of pMSSM models, is discussed.

### 1.3 Search for electroweakinos

While both the ATLAS experiment [88] and CMS experiment [89] at the LHC at CERN set strong limits on the presence of gluinos and squarks at the TeV scale, the limits on electroweakinos are mostly still below 1 TeV. The reason for the relatively low limits on electroweakinos are the low cross-sections of electroweakino production, compared to those of squark and gluino production. As can be seen in fig. 1.8, the cross sections for  $\tilde{\chi}_1^\pm \tilde{\chi}_2^0$  pair production (the main production process considered in the following) is more than two orders of magnitude smaller than that for gluino pair production.

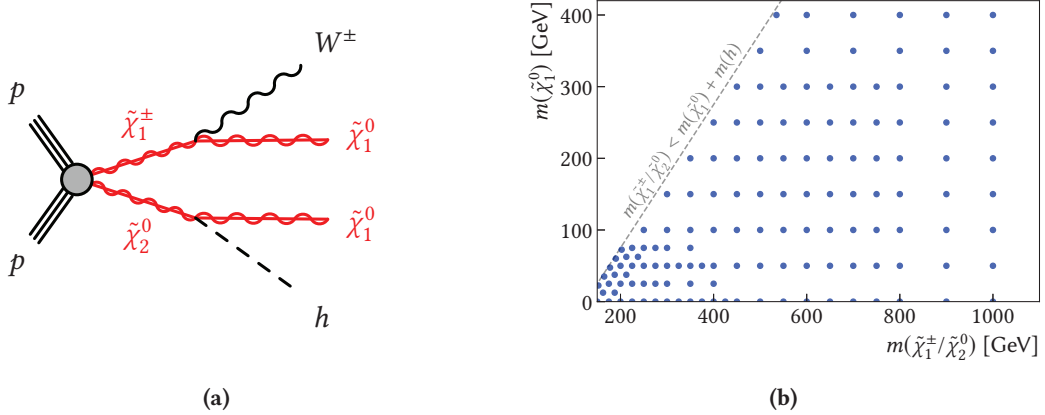


**Figure 1.10:** Simplified model used in this thesis. Fig. (a) shows a diagram for  $\tilde{\chi}_1^\pm \tilde{\chi}_2^0$  pair production with subsequent decays into  $\tilde{\chi}_1^\pm \rightarrow W^\pm \tilde{\chi}_1^0$  and  $\tilde{\chi}_2^0 \rightarrow h\tilde{\chi}_1^0$ . Fig. (b) shows the signal grid used. Each discrete point represents a different signal model with a unique set of  $\tilde{\chi}_1^\pm/\tilde{\chi}_2^0$  and  $\tilde{\chi}_1^0$  mass parameters.

Apart from the electroweakino mass limits set by the current collider experiments, some additional limits from the LEP experiments are still relevant in some corners of the phase space. Combining the results from all four LEP experiments leads to a general lower chargino mass limit of 103.5 GeV, except for scenarios with a low sneutrino mass [90]. For small mass splittings between the chargino and the LSP, the lower limit is a little weaker, with dedicated searches excluding charginos with  $m(\tilde{\chi}_1^\pm) < 91.9$  GeV [90]. For mass splittings larger than 1.5 GeV and up to 50 GeV, the LEP chargino limits have recently been superseded by a dedicated ATLAS search for compressed SUSY scenarios [91], excluding chargino masses up to 240 GeV for a mass splitting of 7 GeV. For the neutralino, a lower limit on the lightest neutralino mass comes from limits on the invisible width of the  $Z$  boson, excluding  $m(\tilde{\chi}_1^0) < 45.5$  GeV, depending on the  $Z$ -neutralino coupling [9].

### 1.3.1 Production of electroweakinos at the Large Hadron Collider

If gluinos and squarks are heavier than a few TeV, i.e. too heavy to be within reach of the LHC, the direct production of electroweakinos might be the dominant production mode of SUSY. At hadron colliders, electroweakinos can be pair-produced directly via electroweak processes. The direct production of electroweakino pairs dominantly happens through electroweak gauge bosons from  $s$ -channel  $q\bar{q}$  annihilation, as shown in fig. 1.9. Contributions from  $t$ -channels via squark exchange are typically of less importance [5].

### 1.3.2 Models used within this work

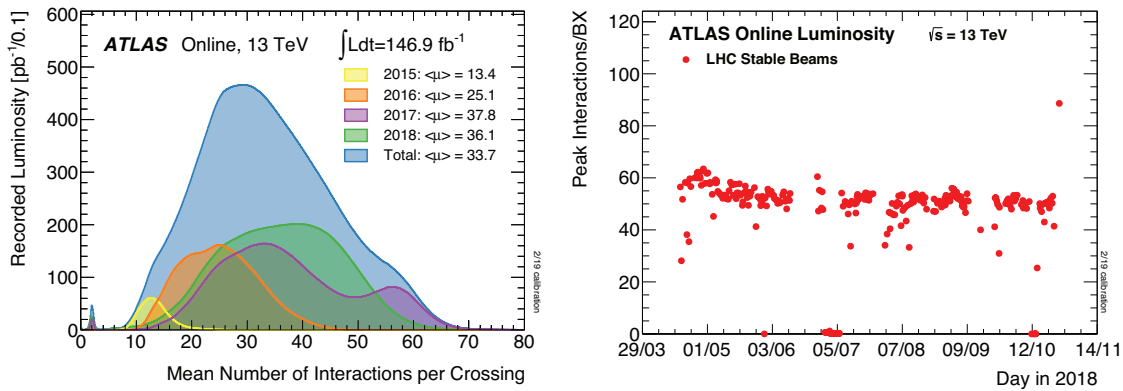
In SUSY scenarios where the sleptons and charged and pseudoscalar Higgs bosons are heavier than the charginos and neutralinos, a relatively pure wino lightest chargino decays predominantly through  $\tilde{\chi}_1^\pm \rightarrow W^\pm \tilde{\chi}_1^0$ , while the next-to-lightest neutralino decays via  $\tilde{\chi}_2^0 \rightarrow Z/h\tilde{\chi}_1^0$ . If, in addition, the higgsinos are much heavier than the wino, and the mass splitting between the two lightest neutralinos is larger than the Higgs boson mass, the decay  $\tilde{\chi}_2^0 \rightarrow h\tilde{\chi}_1^0$  can be the dominant decay mode of the  $\tilde{\chi}_2^0$ . In this case, both the  $\tilde{\chi}_1^\pm$  and  $\tilde{\chi}_2^0$  are wino-like and nearly mass-degenerate.











(a) Luminosity-weighted mean number of interactions per bunch crossing during Run 2 data-taking. (b) Peak mean number of interactions per bunch crossing for each fill during 2018.

**Figure 2.2:** Number of interactions per bunch crossing recorded by the ATLAS experiment. Figures taken from Ref. [107].

30. Figure 2.2(a) shows the mean number of interactions per bunch crossing during the Run 2 data-taking period, weighted by luminosity (a quantity introduced in section 2.1.2) and split up in the different data-taking years. In 2018, for example, the peak number of interactions per bunch crossing  $\mu_{\text{peak}}$  for each fill has been consistently around 50, as shown in fig. 2.2(b).

Experimentally, pile-up can be divided into five major components [108]:

- *In-time* pile-up: multiple interactions during a single bunch crossing, of which not all will be interesting, as often with relatively low energy. If they can be resolved, the main hard-scattering event can still be isolated and studied.
- *Out-of-time* pile-up: additional collisions occurring in bunch crossings before or after the main event of interest. This happens either due to read-out electronics integrating over longer time frames than the 25 ns bunch spacing, or detector components being sensitive to several bunch crossings.
- *Cavern background*: gas of thermal neutrons and photons that fill the experimental caverns during a run of the LHC and tend to cause random hits in detector components.
- *Beam halo events*: protons scraping an up-stream collimator, typically resulting in muons travelling parallel to the beam pipe.
- *Beam gas events*: interactions between proton bunches and residual gas in the beam pipe, typically occurring well outside the main interaction region.

While the effects of cavern background can be mitigated through special pieces of shielding, beam halo and beam gas events leave signatures that can be recognised and removed with high efficiency. Signals from in-time and out-of-time pile-up create irreducible overlap with the events of interest, significantly impacting analyses, and thus need to be taken into account with a dedicated MC simulation [108].













































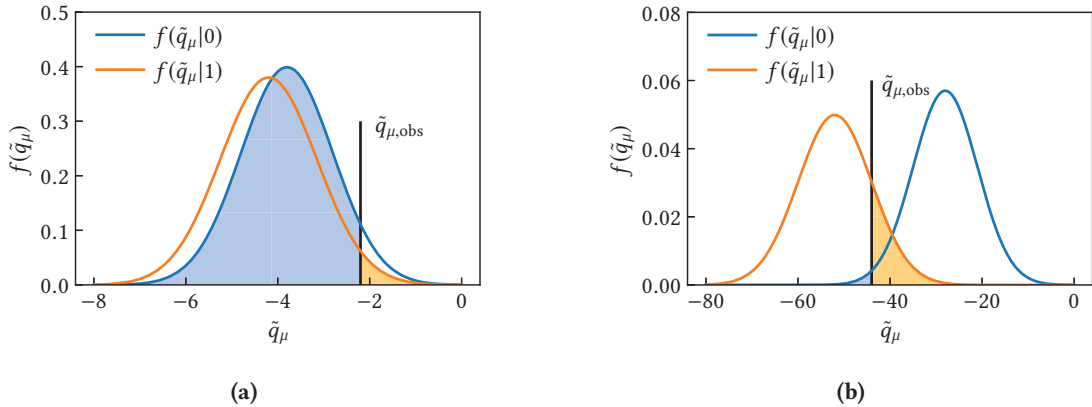


**Figure 3.1:** Distribution of the pdfs of the signal plus background (in orange) and background-only (in blue) models. The orange and blue coloured areas represent the  $p_{s+b}$  and  $p_b$  values, respectively. Figure (a) shows a case where both pdfs are close together, while figure (a) shows a case where they are well separated. Figures created by the author but based on Ref. [175].

### 3.4 $\text{CL}_s$ approach

In the  $\text{CL}_{s+b}$  method, a signal-plus-background model is excluded if  $p_{s+b} < \alpha$ , where  $\alpha$  is defined by the desired confidence level, typically  $\text{CL} = 1 - \alpha = 95\%$ , and  $p_{s+b}$  can be calculated using the test statistic  $\tilde{q}_\mu$  (with  $\mu = 1$ ) introduced in eq. (3.14). If the experiment has very low sensitivity to a specific signal-plus-background model, e.g. because the production cross section of the signal process is too low, the distribution of the test statistic of the signal-plus-background model will be very close to that of the background-only model. In case of an underfluctuation in data, the  $\mu = 1$  model can then be falsely excluded, even though no sensitivity is expected. Figure 3.1 illustrates this with a simple example. In fact, the exclusion of models to which the experiment has no sensitivity has a probability of at least  $\alpha$  [175].

This problem can be remedied by adopting the  $\text{CL}_s$  method [176], altering the threshold for excluding a model in a way to avoid exclusion of models to which the experiment has very low sensitivity. The  $\text{CL}_s$  value is defined as

$$\text{CL}_s = \frac{p_{s+b}}{1 - p_b}, \quad (3.18)$$

where  $p_b$  is the  $p$ -value of the background-only hypothesis<sup>†</sup>. If the distributions of the test statistics for the signal-plus-background and the background-only models are close to each other (as illustrated in fig. 3.1(a)) a small value of  $p_{s+b}$  due to an underfluctuation in data will entail a large value of  $p_b$ . Consequently, in the calculation of the  $\text{CL}_s$  value,  $p_{s+b}$  will be penalised by  $1 - p_b$  (that will be close to 0), resulting in  $\text{CL}_s > p_{s+b}$ , preventing the exclusion of the signal-plus-background model. Conversely, in the case where the two test statistics are well-separated (see fig. 3.1(b)) and  $p_{s+b} < \alpha$ , then  $p_b$  will also be small and thus  $\text{CL}_s$  will be close to  $p_{s+b}$  obtained by the frequentist approach.

<sup>†</sup> It is worth highlighting that  $p_b$  is equal to  $p_\mu$  from eq. (3.15) with  $\mu = 0$ . This is strictly different from  $p_0$  in eq. (3.11) as it relies on a different test statistic.







































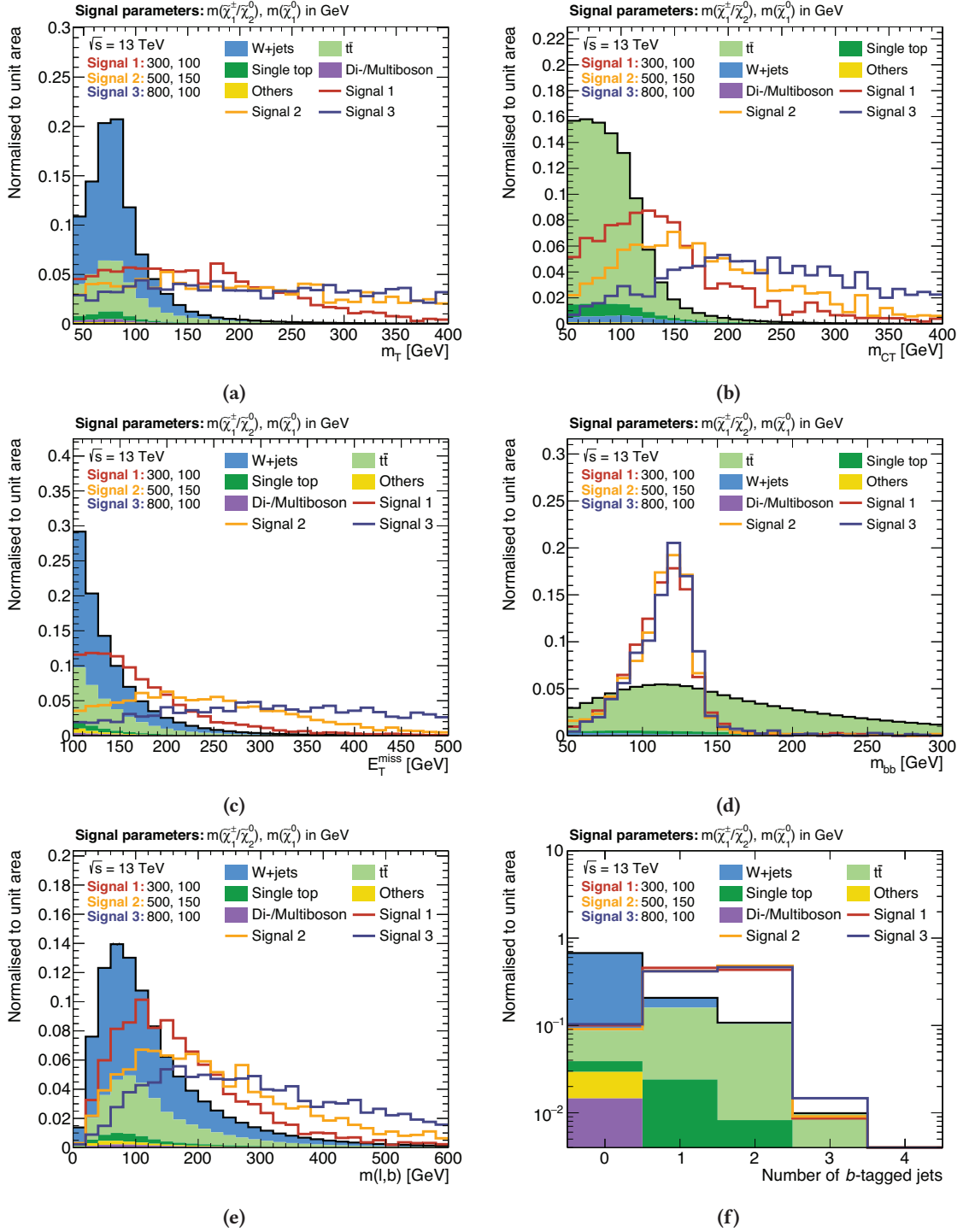


**Figure 4.3:** Distributions of the most important observables used in the analysis. The simulated SM backgrounds are stacked on top of each other, and distributions from exemplary signal models with the quoted mass parameters are overlaid. In order to emphasise the shape differences, both total background and signal distributions are normalised to unity. A preselection of a lepton (electron or muon), at least two jets and  $E_T^{\text{miss}} > 100$  GeV is applied.



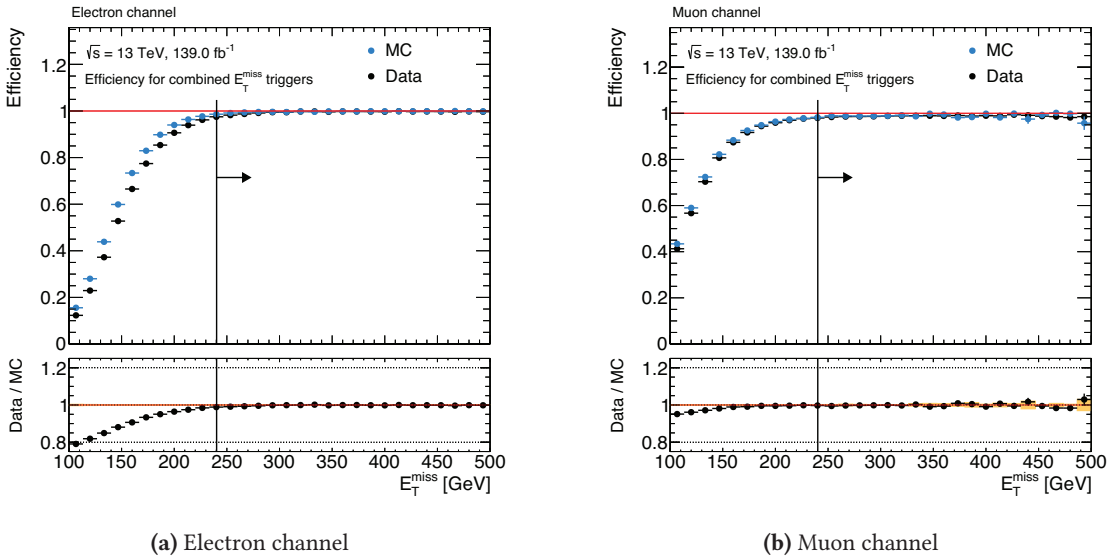


**Figure 4.4:** Efficiencies of the combined  $E_T^{\text{miss}}$  triggers in data and MC events, triggered by single lepton triggers in the (a) electron and (b) muon channels. A preselection requiring an electron or muon, at least two jets, and  $E_T^{\text{miss}} > 100 \text{ GeV}$  is applied on all events. The arrow indicates the offline  $E_T^{\text{miss}}$  requirement applied on all selections in the analysis.

thus corrected for pile-up effects [243]. The pufit algorithm was used during the 2017–2018 data taking period and takes as input topo clusters, formed using the method described in section 4.4.2. The clusters are subsequently combined into  $\eta$ - $\phi$  patches of size corresponding approximately to that of a jet with  $R = 0.4$ . A correction for pile-up effects, based on the distribution of the energy deposits in the calorimeter, is applied on the clusters. The pufit algorithm assumes that high  $E_T$  deposits stem from the hard-scatter events while low  $E_T$  deposits originate mostly from pile-up effects [242]. The online  $E_T^{\text{miss}}$  threshold of the triggers increased from 70 GeV to 110 GeV in order to keep the trigger rate more or less stable under the rising instant luminosities during the different data-taking periods.

Due to resolution effects arising in the combination of the L1 and HLT triggers, and differences in the online reconstruction techniques compared to those used in offline physics analysis, the performance of triggers is in general not a simple step function but consists of a so-called *turn-on curve* with rising efficiency, followed by a *plateau region* with constant efficiency. In order to achieve the same trigger selection in MC as in data, the MC events are each assigned a random run number that are distributed according to the respective integrated luminosities of each data taking period. Using these run numbers, the same triggers used for data-taking during each run can be applied for MC events.

Figure 4.4 shows the combined  $E_T^{\text{miss}}$  trigger efficiencies for the electron and muon channels separately. In the following, an offline requirement of  $E_T^{\text{miss}} > 240 \text{ GeV}$  is applied for all analysis regions, selecting events where the  $E_T^{\text{miss}}$  triggers are fully efficient and no significant difference between MC and data is observed. Thus, no trigger efficiency correction is considered in the following. A statistical uncertainty of 2% is used to account for the difference between data and MC in the trigger plateaus.





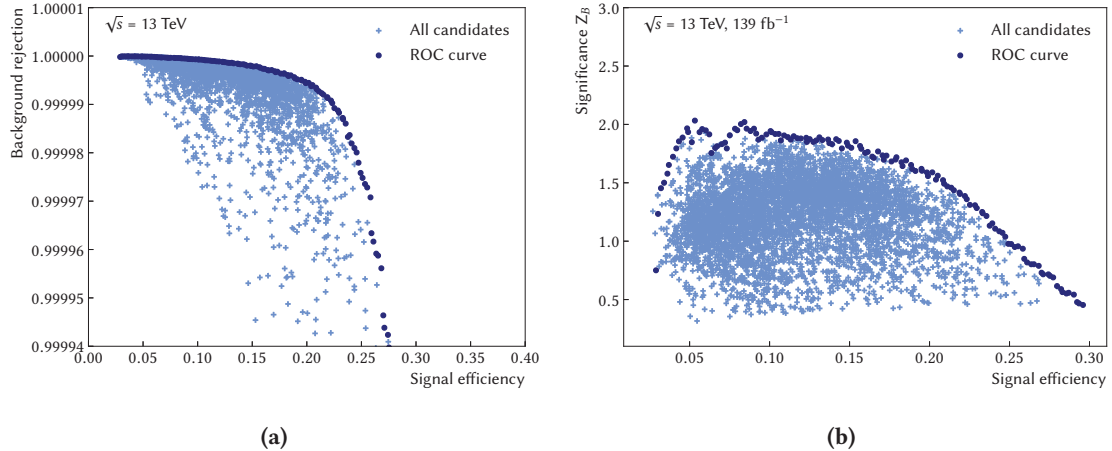


**Figure 5.1:** Small  $N$ -dimensional cut scan using  $10^4$  unique cut combinations, illustrating the approach of (a) generating a ROC curve from the scanned cut combinations in order to (b) reduce the number of candidates used in computationally expensive significance calculations. The cut combination candidates forming the ROC curve (dark blue) also maximise the discovery significance. In (b), the significance  $Z_B$  includes the MC statistical uncertainty on the expected background rate and a constant 30% systematic uncertainty.

is that, for a fixed signal efficiency, the cut combination candidate maximising the background rejection also maximises the discovery significance  $Z_B$ . With the significance definition used herein, this is in general a valid assumption, as the significance tends to monotonically increase with decreasing background rate, even while the statistical uncertainty on the background estimation increases due to tighter requirements and less available MC statistics (cf. fig. 5.1). This procedure effectively generates a ROC curve, that can be used to perform more computationally intensive calculations, as e.g. calculating different variations of the discovery significance. The approach is illustrated in a small scan using  $10^4$  cut combinations in fig. 5.1. The cut combination candidates maximising the background rejection and thus lying on the ROC curve in fig. 5.1(a) are the same candidates that maximise the discovery significance in fig. 5.1(b).

A common problem of  $N$ -dimensional scans is the concept of *overtightening* the selections given the available MC statistics. Since the cross sections of the SUSY processes considered are many orders of magnitude smaller than those of the dominant SM processes, it is often necessary to apply tight requirements on the kinematic observables in order to achieve a significant signal-to-background separation. However, due to the finite amount of MC statistics available, many of the more extreme cut combinations select kinematic regions where not enough MC statistics are available for a reasonable estimation of the background rates. Thus, by maximising the background rejection, it may occur that cut combinations are selected where the mere lack of MC statistics, needed to properly estimate the background rates, causes a high significance value. As the significance values obtained for such configurations are obviously not trustworthy, they need to be avoided.

In the  $N$ -dimensional cut scan implementation used herein, the available MC datasets are split in two statistically independent, equally sized subsets. Although resulting in an additional dilution of the available MC statistics, this approach allows to generate two independent ROC curves and to compute two independent values for the discovery significance for each cut combination





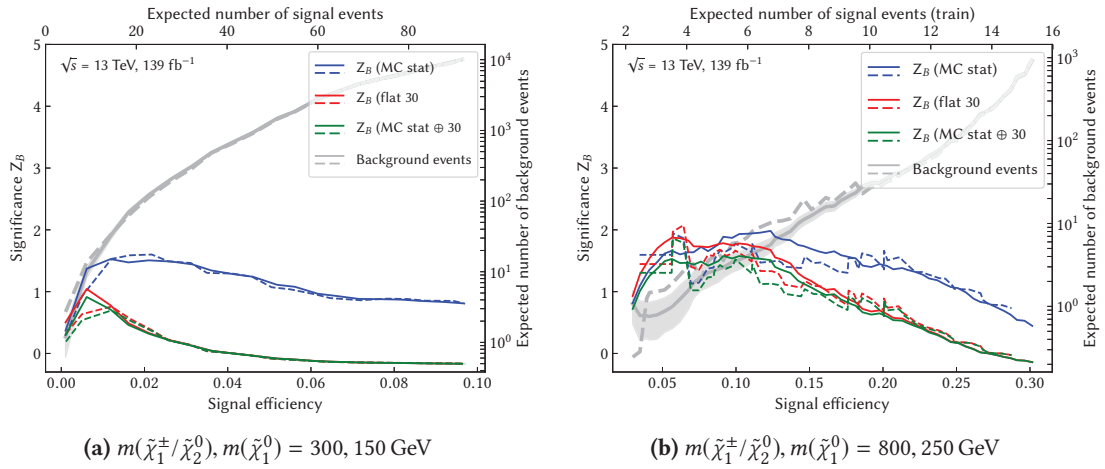


**Figure 5.2:** Results of the  $N$ -dimensional cut scan for two exemplary benchmark points. The binomial discovery significance  $Z_B$  is plotted against the signal efficiency for different uncertainty configurations. Additionally, the expected SM background event rates are shown (grey), including their statistical uncertainties for one of the two statistically independent samples (grey shaded area). The solid and dashed lines represent the two statistically independent subsets that the MC samples are split into.

of the detector. Events with a large share of fake  $E_T^{\text{miss}}$  accumulate at low values of  $\mathcal{S}$ , while events with mostly real  $E_T^{\text{miss}}$  tend to have large values of  $\mathcal{S}$ .

- The distance between the two leading jets  $\Delta R_{jj}$  as well as between the two  $b$ -jets  $\Delta R_{bb}$ . Especially in events with a large mass difference between the electroweakinos, the Higgs can receive a significant boost, such that the two  $b$ -jets from the Higgs decay tend to be close together in the laboratory frame (and are also the highest- $p_T$  jets in an event), resulting in small values of both  $\Delta R_{jj}$  and  $\Delta R_{bb}$ . In SM background processes, however, the two leading ( $b$ -)jets often do not originate from the same object and thus tend to be further apart.
- The azimuthal distance between the lepton  $p_T$  and the missing transverse momentum, denoted by  $\Delta\phi(\mathbf{p}_T^\ell, \mathbf{p}_T^{\text{miss}})$ . This observable exploits the fact that the lepton and the  $E_T^{\text{miss}}$  tend to have a more back-to-back configuration in signal events than in many SM processes where the lepton and the neutrino (the latter often responsible for a large part of the  $E_T^{\text{miss}}$  in an event) often originate from the same  $W$  boson decay.

In order to avoid selecting cut combination candidates with overtightened selection criteria compared to the available MC statistics, constraints are applied on the relative statistical uncertainty on the background, and on the number of unweighted MC events passing the cut combination candidates. Cut combinations are only considered if they result in less than 50% relative statistical uncertainty on the total background. In addition, all cut combinations need to result in at least five unweighted MC events for each of the three major backgrounds,  $t\bar{t}$ , single top and  $W + \text{jets}$ .

The discrete selection possibilities for each of the observables are shown in table 5.1. A preselection of a lepton and exactly two  $b$ -jets (and thus at least two jets overall in the event) is always applied. Requirements on the different observables in table 5.1 are optional and do not need to be applied by the optimisation algorithm. The results of the brute-force  $N$ -dimensional cut scans for each benchmark signal point can be visualised by plotting the expected discovery significance  $Z_B$



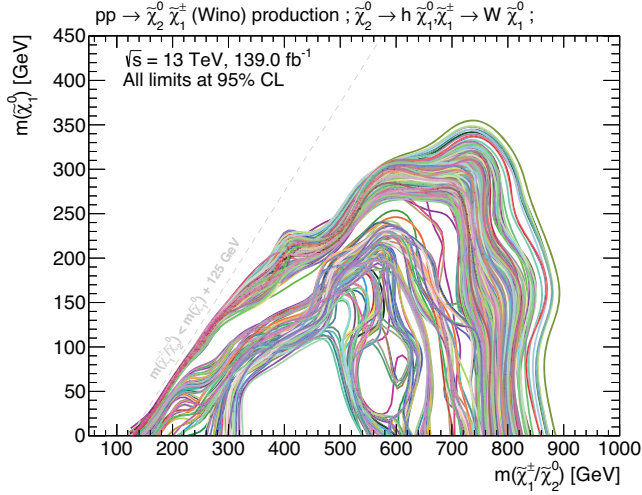


**Figure 5.3:** Expected exclusion contours obtained from a subset of the signal region candidates. The background estimate is directly taken from MC and includes MC statistical uncertainty as well as an uncorrelated scale uncertainty of 30%. For the sake of visibility, only the nominal contours are shown (without uncertainty bands). Configurations resulting in multiple, disjoint patches of excluded areas are rejected.

in a single likelihood and can be used in a simultaneous fit to data, effectively creating a two-dimensional shape-fit in these observables. Such a shape-fit configuration allows to exploit the differences in shape between signal and background distributions, and is able to accommodate the varying shapes of signal points from different regions in the parameter space, making it an ideal statistical tool to cover a wide range of kinematic regimes.

The optimal number of bins as well as values of the individual bin edges in both distributions depends on the available MC statistics and is determined using the simplified fit scans introduced in section 5.1.3. The MC statistical uncertainties, as well as a systematic uncertainty of 30%, correlated over all bins, are considered in each configuration. The number of bins is varied in each direction ( $m_T$  and  $m_{CT}$ ) between two and five using different bin edges, varied within ranges determined by the optimal cut values obtained for the benchmark points. As configurations with more bins could, in some circumstances, potentially benefit from the additional MC statistics resulting from looser selection criteria on the remaining variables, the previously consolidated baseline selection is also allowed to vary to some extent. Finally, although not expected to yield better performance, configurations with multiple orthogonal signal region bins in  $E_T^{\text{miss}}$  or  $m_{b\bar{b}}$  are also included in the scan. A subset of the investigated candidates is illustrated in fig. 5.3, showing the nominal expected exclusion limit at 95% without uncertainty bands. Configurations with multiple, disjoint patches of excluded areas in the parameter space are discarded, as they typically result from high statistical fluctuations.

As expected from table 5.2, the best performing configurations define multiple signal region bins in the  $m_T$  and  $m_{CT}$  distributions, while keeping a constant baseline selection on the remaining observables. Figure 5.4(a) shows a comparison of the expected exclusion contour for exemplary two-dimensional shape-fit configurations, using signal regions binned in  $(m_T, E_T^{\text{miss}})$ ,  $(m_T, m_{b\bar{b}})$  or  $(m_T, m_{CT})$ . The setup using a two-dimensional shape-fit in  $m_T$  and  $m_{CT}$  clearly maximises the expected excluded area. Finally, applying a requirement on high values of  $m_{\ell b_1}$  in the highest  $m_T$  bins has been shown (cf. fig. A.9) to further increase sensitivity to signal models with high mass differences.

In fig. 5.4(b), the fully optimised two-dimensional shape-fit configuration is compared with the signal regions of the previous iteration of the search [180], scaled up to the integrated luminosity

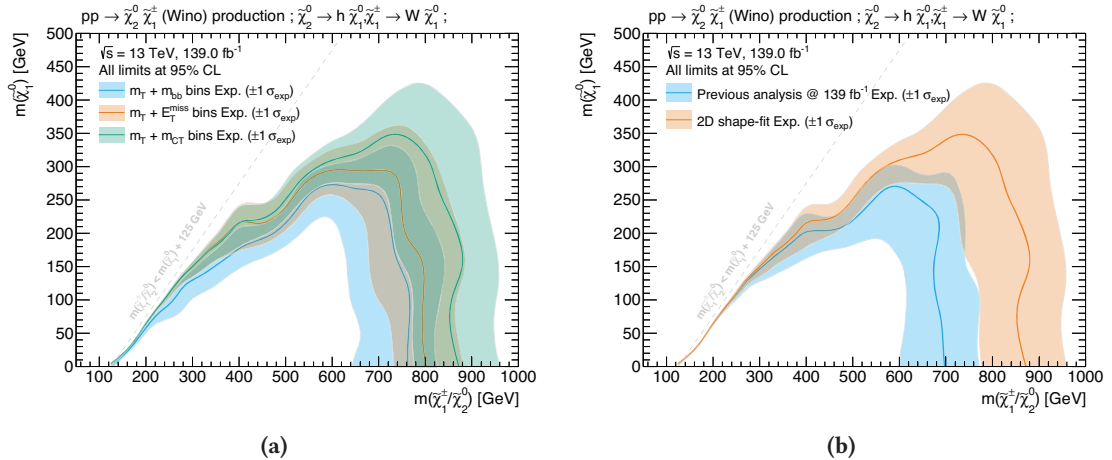


**Figure 5.4:** Comparison of different shape-fit configurations. Figure (a) compares three different two-dimensional shape-fit configurations using  $3 \times 3$  bins in  $(m_T, E_T^{\text{miss}})$ ,  $(m_T, m_{bb})$  and  $(m_T, m_{CT})$ . Figure (b) compares the two-dimensional shape-fit in  $m_T$  and  $m_{CT}$  to the signal regions of the previous analysis iteration signal regions scaled to  $139 \text{ fb}^{-1}$ . All exclusion limits shown are expected limits at 95% CL, using MC statistical and 30% systematic uncertainties.

of the full Run 2 dataset. It can clearly be seen that a significant improvement in sensitivity is achieved through the introduction of the two-dimensional shape-fit strategy.

### 5.3 Signal region definitions

An overview of the final signal region definitions is provided in table 5.3. Based on the previously discussed results, three signal regions bins in  $m_T$  are defined, optimised for different regimes in the  $\tilde{\chi}_1^\pm/\tilde{\chi}_2^0$  and  $\tilde{\chi}_1^0$  mass difference. According to the mass difference regime targeted, they are aptly called low (SR-LM), medium (SR-MM), and high (SR-HM) mass signal regions, respectively. While SR-LM targets the smallest values of  $m_T$ , SR-MM and SR-HM target progressively increasing values of  $m_T$ . All three signal regions are further divided into three  $m_{CT}$  bins each, resulting in a total of nine disjoint signal region bins. The signal region with the highest requirement on  $m_T$  (SR-HM) also requires  $m_{\ell b_1} > 120 \text{ GeV}$ , for the reason explained previously. All three signal regions otherwise share a common set of requirements on the number of jets,  $E_T^{\text{miss}}$  and  $m_{bb}$ . As shape-fits are by construction highly model-dependent<sup>†</sup>, these SRs will be used for deriving model-dependent limits in the case where no significant excess, compared to the expected SM background rate, is seen in data. For this reason, the shape-fit regions will be referred to as *exclusion* regions in the following. A graphical representation of the nine exclusion signal region bins is shown in fig. 5.5. The kinematic distributions in SR-LM, SR-MM and SR-HM are shown as  $N-1$  plots in figs. 5.6 to 5.8.

For evaluating a potential excess in data compared to the expected background rate, a second set of signal regions is derived from the optimised shape-fit setup. For each of the three bins in the transverse mass (SR-LM, SR-MM, and SR-HM), the three  $m_{CT}$  bins are summed up and the upper

<sup>†</sup> The signal shapes need to be known in order to estimate the expected signal rates in multiple, disjoint signal region bins.



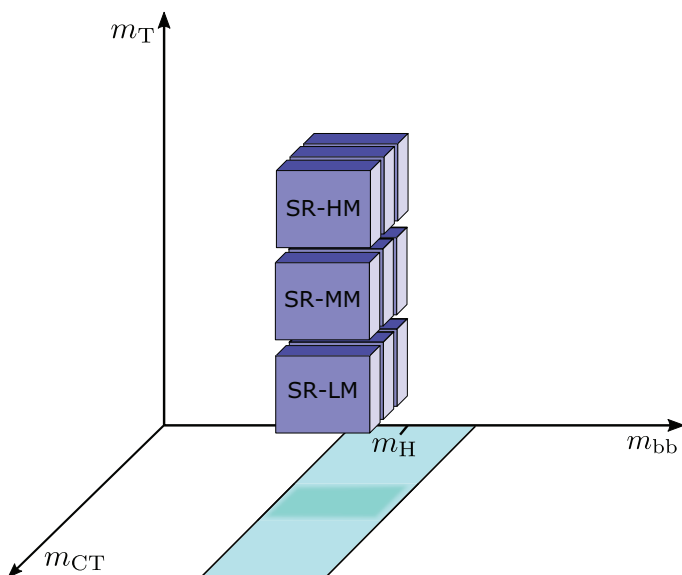


**Figure 5.5:** Configuration of the exclusion signal regions. Nine signal region bins are defined in  $m_T$  and  $m_{CT}$  within the Higgs mass window. All signal regions can be statistically combined using a single likelihood, effectively resulting in a two-dimensional shape-fit.

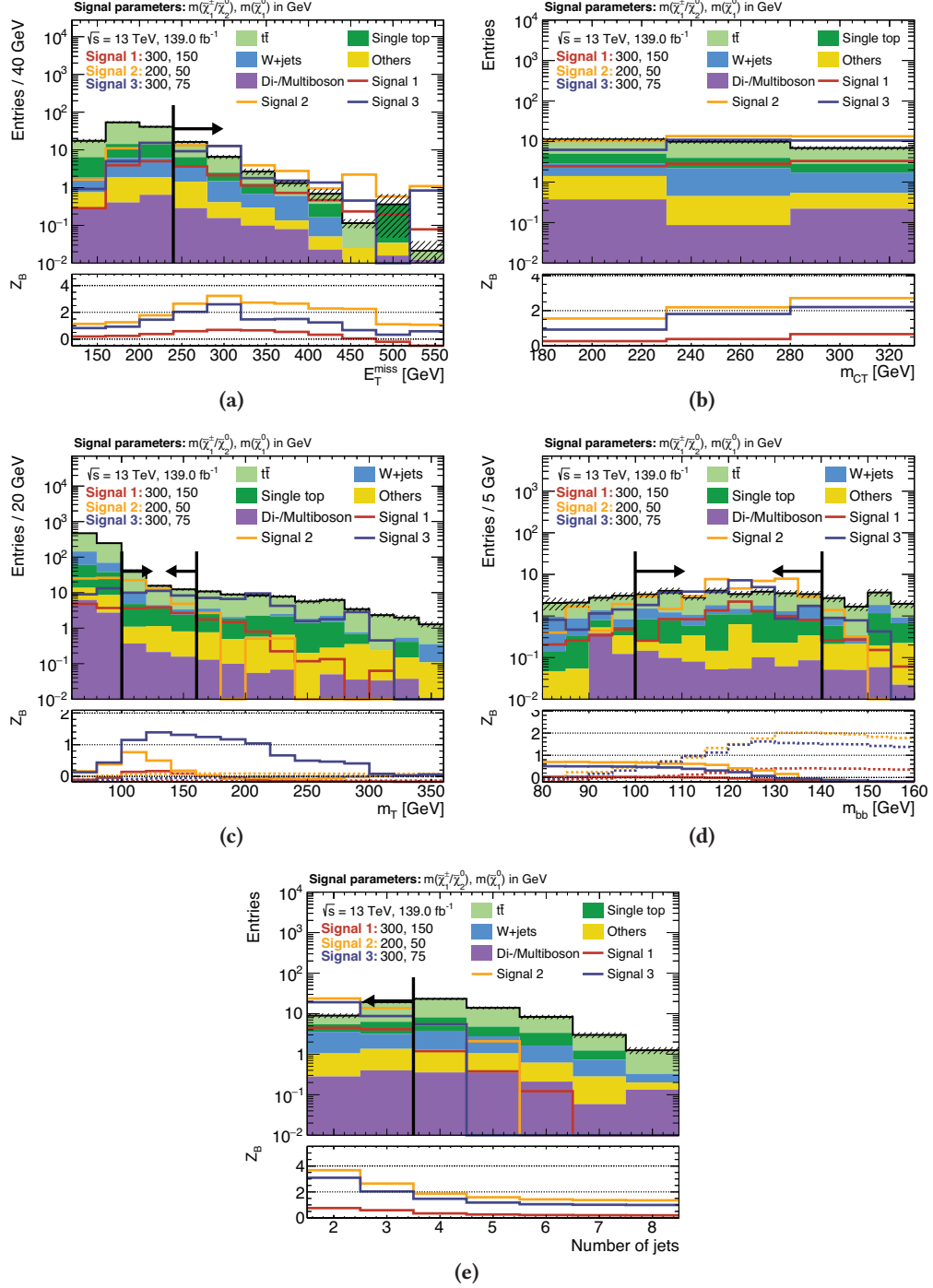


**Figure 5.6:**  $N-1$  plots for SR-LM, with exemplary signal points and all  $m_{\text{CT}}$  bins included. The dashed area represents the MC statistical uncertainties on the background. In all figures except fig. (b), the significance in the lower pad is obtained by summing up all the events in the direction of the cut arrow and includes 30% systematic uncertainties as well as MC statistical uncertainties. In fig. (b) the significance is only computed on a bin-by-bin basis, i.e. not summing up all events in the direction of the cut arrow.

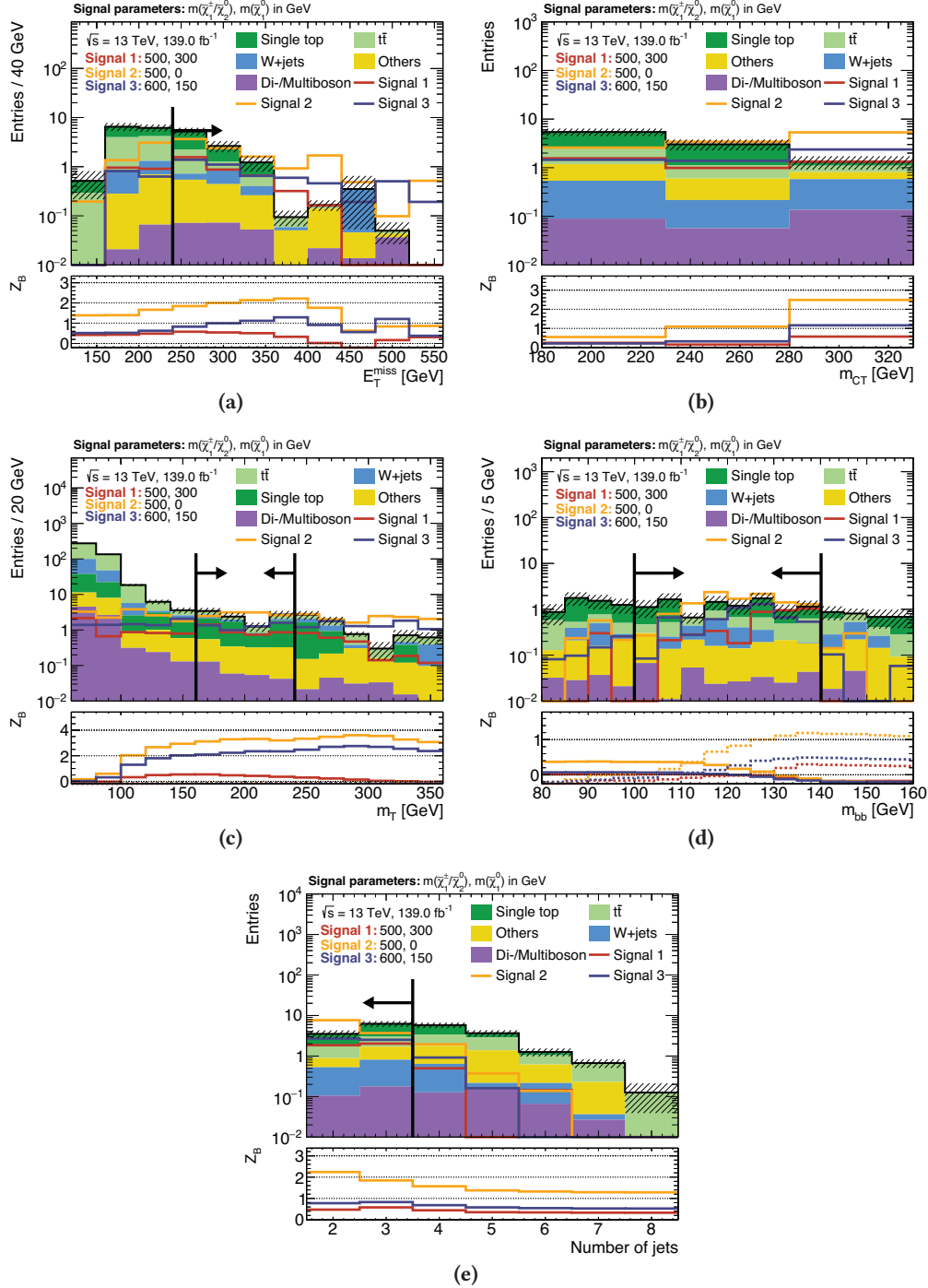


**Figure 5.7:**  $N-1$  plots for SR-MM, with exemplary signal points and all  $m_{\text{CT}}$  bins included. The dashed area represents the MC statistical uncertainties on the background. In all figures except fig. (b), the significance in the lower pad is obtained by summing up all the events in the direction of the cut arrow and includes 30% systematic uncertainties as well as MC statistical uncertainties. In fig. (b) the significance is only computed on a bin-by-bin basis, i.e. not summing up all events in the direction of the cut arrow.

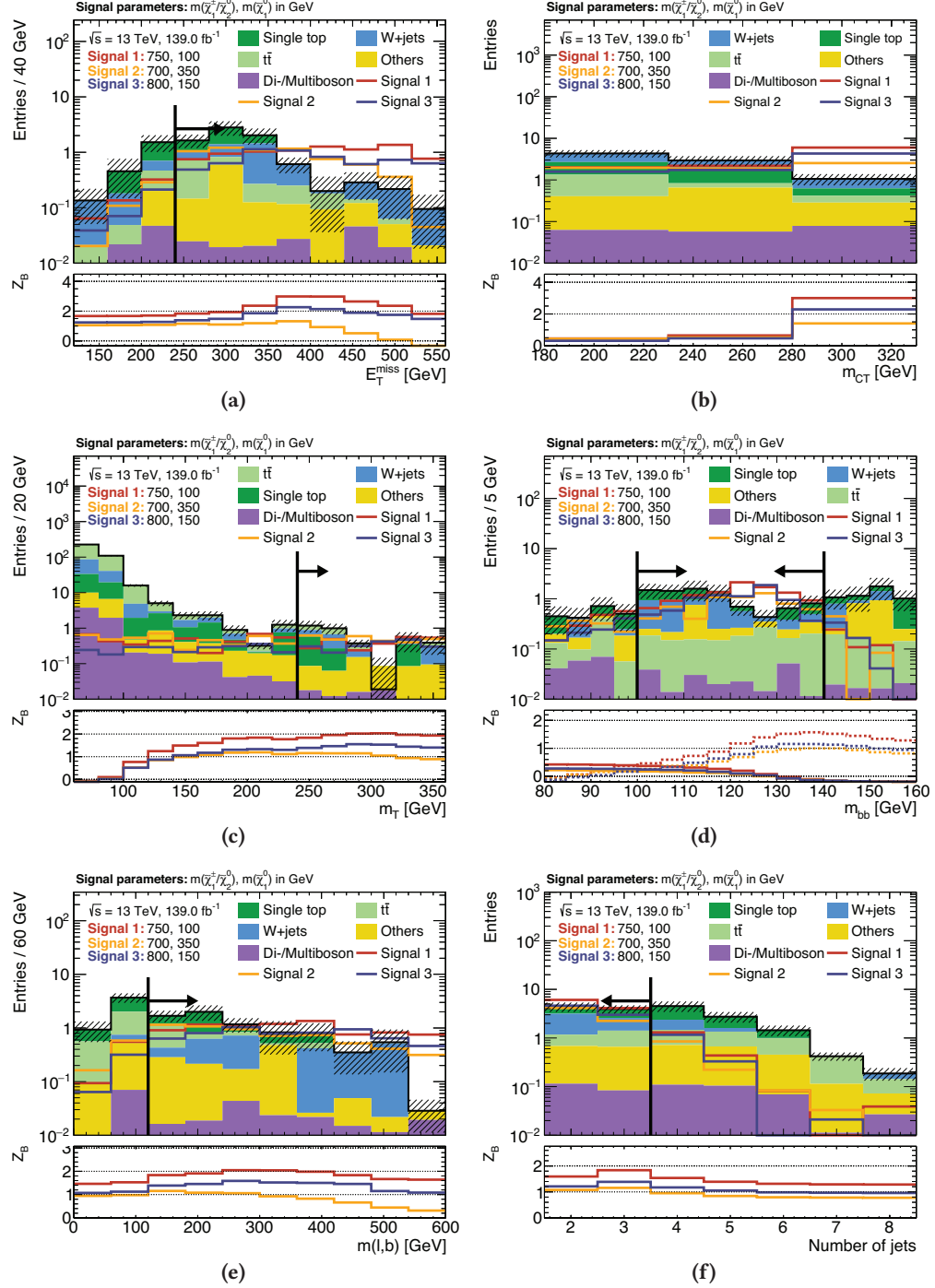


**Figure 5.8:**  $N-1$  plots for SR-HM, with exemplary signal points and all  $m_{CT}$  bins included. The dashed area represents the MC statistical uncertainties on the background. In all figures except fig. (b), the significance in the lower pad is obtained by summing up all the events in the direction of the cut arrow and includes 30% systematic uncertainties as well as MC statistical uncertainties. In fig. (b) the significance is only computed on a bin-by-bin basis, i.e. not summing up all events in the direction of the cut arrow.













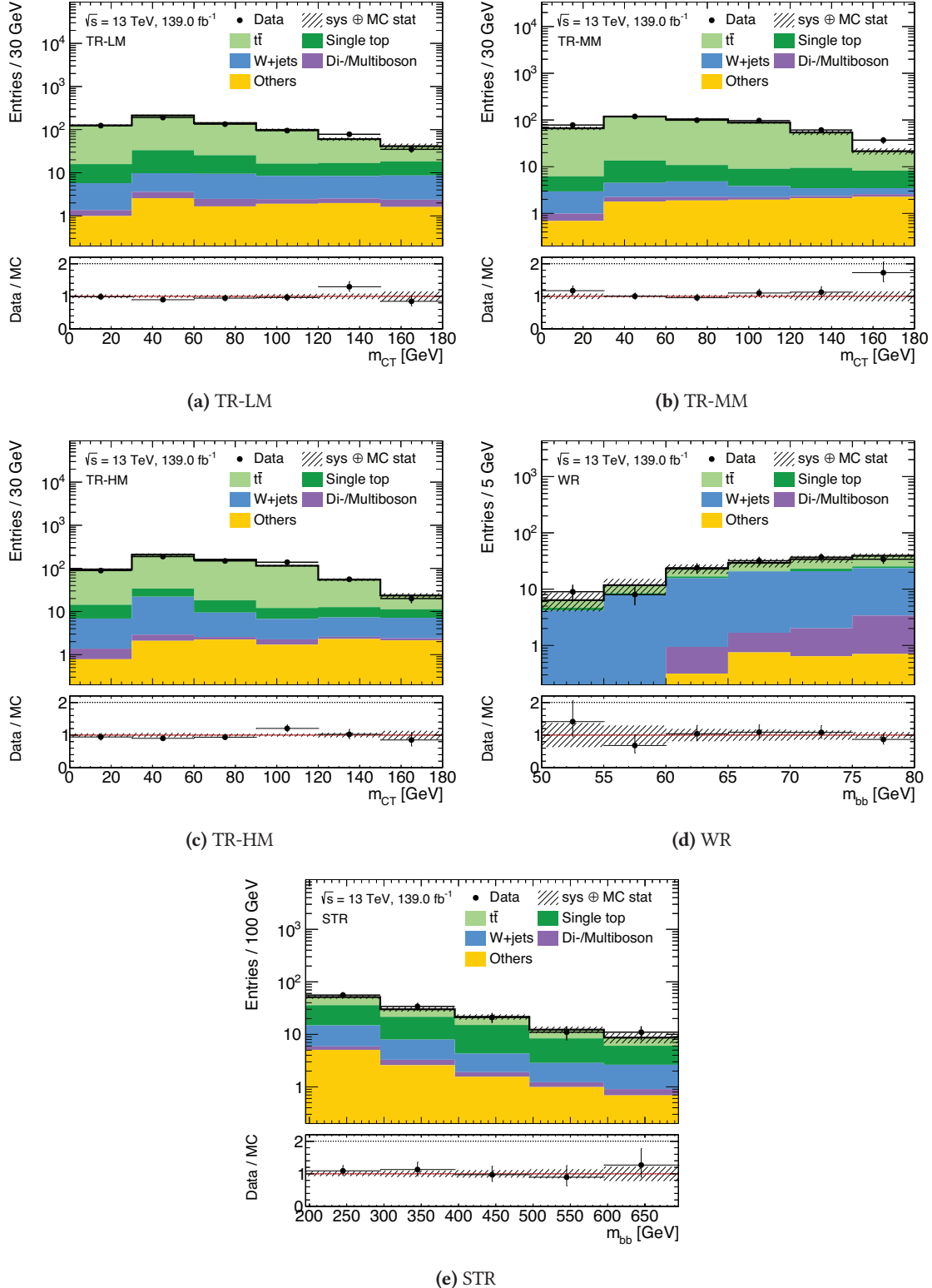


**Figure 6.2:** Exemplary pre-fit distributions for each control region. As laid out in the beginning of this chapter, the shaded region includes MC statistical uncertainty as well as experimental uncertainties, added in quadrature. The dominant backgrounds are normalised using the procedure described in section 6.1.3. A good agreement between MC expectation and data is observed in all CRs.

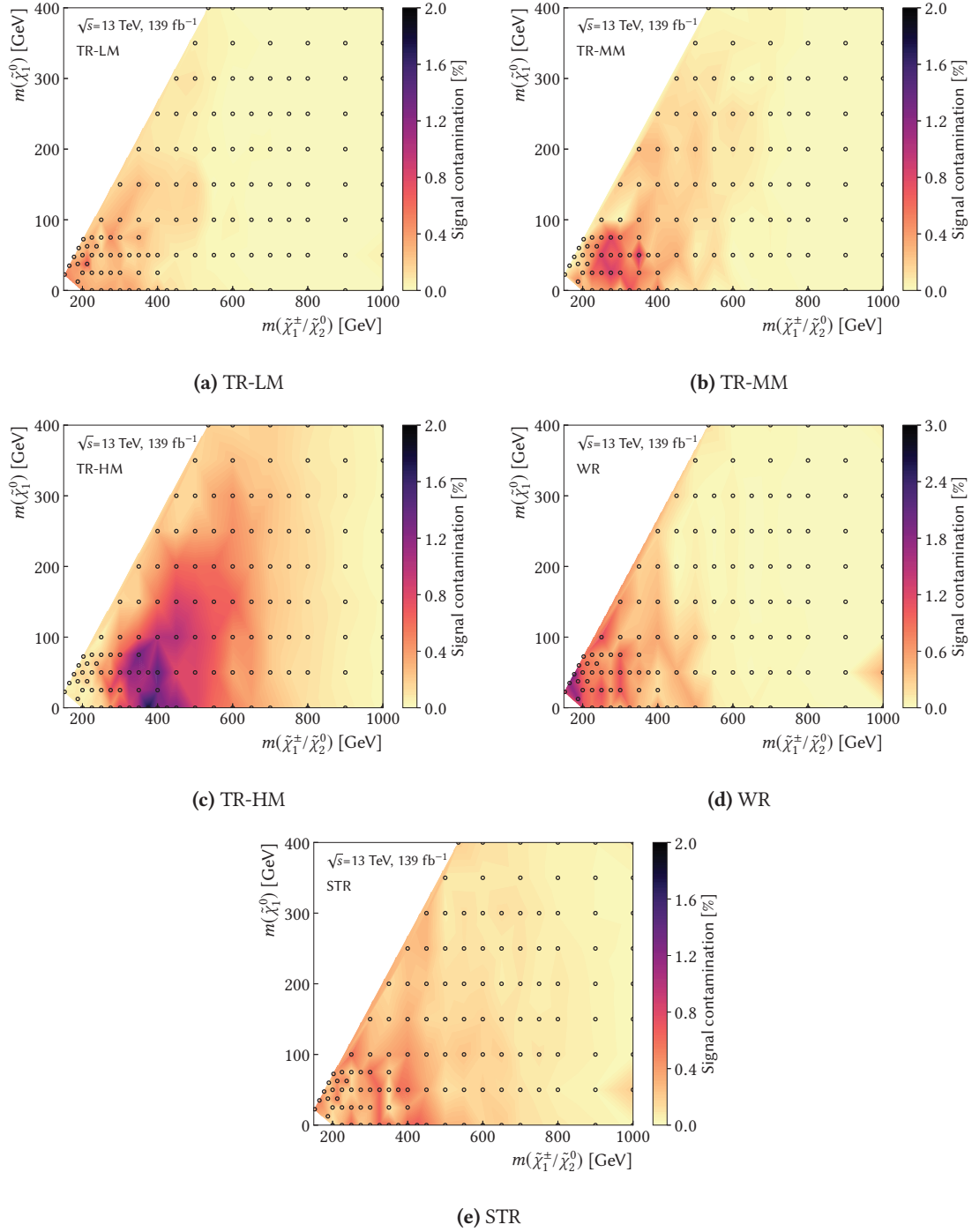


**Figure 6.3:** Signal contamination for all CRs throughout the signal grid. The space between the signal points (indicated by the black circles) is interpolated using Delaunay triangles.

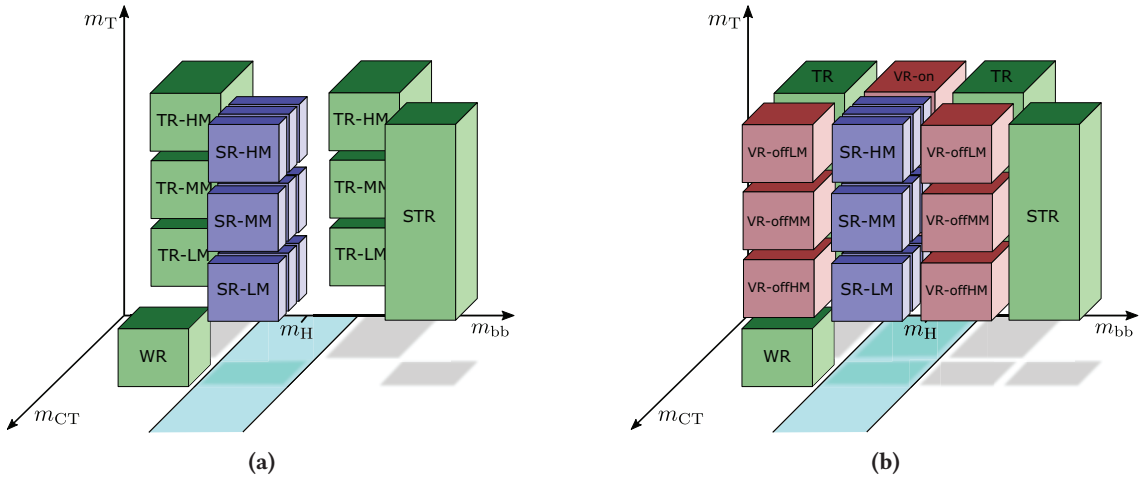


**Figure 6.4:** Configuration of (a) the CRs placed around the SRs off the  $m_{bb}$  window and (b) the validation regions in the phase space between the CRs and SRs. The VRs are arranged such that each of the extrapolations can be validated separately for SR-LM, SR-MM and SR-HM.

### 6.3 Validation regions

Two sets of validation regions are introduced in order to verify the extrapolations over the different distributions. The selections defining all VRs are summarised in table 6.1. The first set, called VR-on is situated on the Higgs boson mass peak but with the  $m_{CT}$  requirement inverted to  $m_{CT} < 180$  GeV. This allows the VR-on regions to validate the extrapolation over  $m_{bb\bar{b}}$ , performed when extrapolating the background estimate from the control regions into the signal regions. Three disjunct VR-on regions are introduced, with  $m_T$  requirements matching those of the SRs, such that the extrapolations can be validated separately for each signal region. The three VR-on regions are aptly named VR-onLM, VR-onMM and VR-onHM. A similar composition of  $t\bar{t}$  decay modes as in the control and signal regions is observed in the VR-on regions, necessary for a trustworthy validation of the  $t\bar{t}$  estimate. A maximum signal contamination of about 5%–14% is achieved, depending on the requirement in  $m_T$ . As can be seen from fig. A.10, most signal points have a signal contamination well below 5% for all VR-on regions.

The second set of validation regions is located on both sides off the Higgs boson mass peak at same values in  $m_{CT}$  than the SRs. This set of *off-peak* VRs, called VR-off, is used to validate the extrapolation over the  $m_{bb\bar{b}}$  distribution performed in the case of STR. Additionally, the VR-off regions validate the extrapolation over  $m_{CT}$ , performed in the  $t\bar{t}$  control regions. Similar to the on-peak validation regions, the VR-off regions are split into  $m_T$  bins matching the signal regions, allowing a validation of the background estimate in their respective signal region. The bins in VR-off are called VR-offLM, VR-offMM and VR-offHM. The maximum signal contamination in the VR-off regions is found to be about 7%–13%, depending on the requirement on  $m_T$ . Most signal points, however, reveal a signal contamination in the VR-off regions of less than 3% (cf. fig. A.10).





































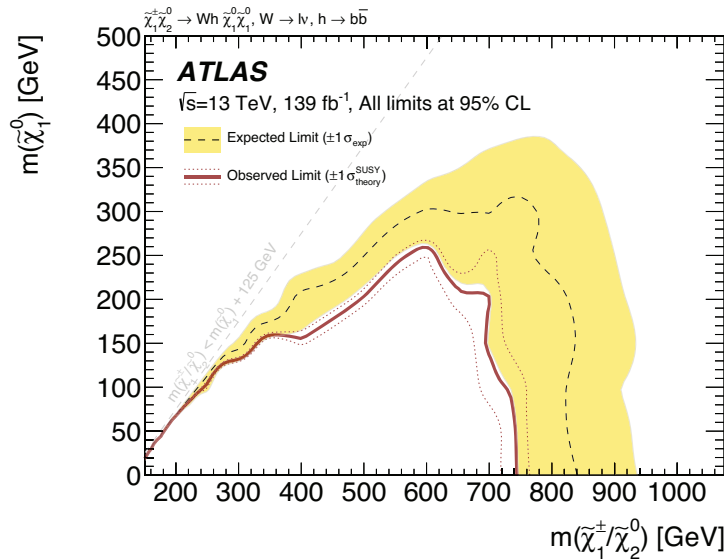


**Figure 8.5:** Model-dependent exclusion contour on  $\tilde{\chi}_1^\pm/\tilde{\chi}_2^0$  pair production. The dashed black line represents the expected limit obtained using Asimov data. The uncertainties are given by the yellow band. The red solid line represents the observed limit obtained using  $139 \text{ fb}^{-1}$  of data taken by ATLAS. By varying the signal cross sections up and down by their uncertainty, the red dashed lines are obtained. All contours are given at 95% CL. Figure adapted from Ref. [182].

### 8.2.2 Model-dependent exclusion limits

For each signal point in the signal grid considered, a separate model-dependent *exclusion* fit is run using all control regions and exclusion signal regions. As all exclusion signal region bins are mutually exclusive, a likelihood containing terms for all nine signal region bins can be constructed, effectively creating a shape-fit in the binned variables  $m_T$  and  $m_{CT}$  (cf. chapter 5). As opposed to the background-only fit, the model-dependent exclusion fits allow for signal contribution in all regions. For each point in the signal grid, the expected and observed  $\text{CL}_s$  values are calculated using the method discussed in section 3.4. Expected (observed) contour lines can then be drawn at expected (observed)  $\text{CL}_s = 0.05$  in the  $m(\tilde{\chi}_1^\pm/\tilde{\chi}_2^0)-m(\tilde{\chi}_1^0)$  plane spanned by the simplified model parameters. Signal points inside the contour are excluded at 95% CL. Figure 8.5 shows the exclusion contours obtained in the signal grid considered for the  $\tilde{\chi}_1^\pm\tilde{\chi}_2^0$  simplified model in the  $1\ell$  search. The dashed black line corresponds to the expected exclusion contour, obtained using the Asimov dataset. The yellow uncertainty band represents the interval containing 68% of all exclusion contours obtained for repeated observations distributed according to the background-only hypothesis. The solid red line represents the observed exclusion limit obtained using the data recorded by ATLAS. As discussed in section 7.2.2, the dashed red lines are obtained by varying the signal cross sections up and down by  $1\sigma$ .

Due to the slight overfluctuations of data observed in some of the exclusion signal region bins, the observed limit is slightly weaker than the expected one. The observed exclusion limit extends to about 740 GeV in  $m(\tilde{\chi}_1^\pm/\tilde{\chi}_2^0)$  for models with a massless  $\tilde{\chi}_1^0$ , and up to 600 GeV in  $m(\tilde{\chi}_1^\pm/\tilde{\chi}_2^0)$  for models with  $m(\tilde{\chi}_1^0) \simeq 250 \text{ GeV}$ . This extends the previous limit set by ATLAS in this simplified

<sup>†</sup> The signal strength is in principle allowed to exceed unity in order for the scan to find a 95% CL upper limit

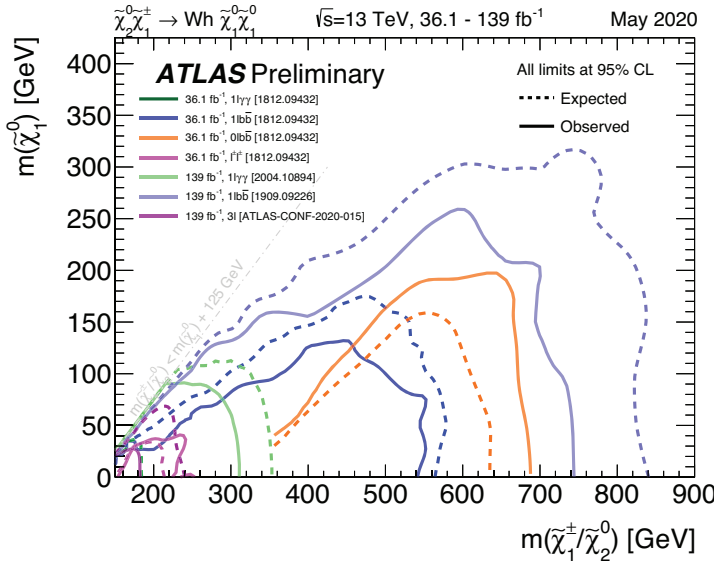


**Figure 8.6:** Summary of ATLAS limits on  $m(\tilde{\chi}_1^\pm/\tilde{\chi}_2^0)$  masses in the  $\tilde{\chi}_1^\pm\tilde{\chi}_2^0 \rightarrow Wh\tilde{\chi}_1^0\tilde{\chi}_1^0$  simplified model. The exclusion limit obtained by the analysis presented in this work is referred to as *1Lbb* (the  $139\text{ fb}^{-1}$  iteration, drawn in light blue) and is the most stringent limit in this simplified model set by an ATLAS search thus far. Figure adapted from Ref. [88].

model and decay channel by more than 200 GeV in  $m(\tilde{\chi}_1^\pm/\tilde{\chi}_2^0)$  for a light  $\tilde{\chi}_1^0$ , an improvement made possible not only by the significant increase in integrated luminosity but also by the introduction of a two-dimensional shape fit in the analysis strategy (cf. fig. 5.4(b)).

### 8.3 Discussion

At the time of writing, the limits derived in this analysis are the most stringent limits on the  $\tilde{\chi}_1^\pm\tilde{\chi}_2^0 \rightarrow Wh\tilde{\chi}_1^0\tilde{\chi}_1^0$  simplified model set by an ATLAS search, surpassing not only the previous iteration of the analysis [180], but also yielding more stringent limits than those published by ATLAS in other decay channels of the same simplified model [88]. Figure 8.6 shows a summary of results published by ATLAS searches in the  $\tilde{\chi}_1^\pm\tilde{\chi}_2^0 \rightarrow Wh\tilde{\chi}_1^0\tilde{\chi}_1^0$  simplified model. Recently, a CMS search for SUSY, interpreted using the same simplified model and targeting the  $1\ell$  final state has excluded  $m(\tilde{\chi}_1^\pm/\tilde{\chi}_2^0)$  masses up to 820 GeV for a massless LSP [255].

Various other searches for SUSY at both ATLAS and CMS are constraining a multitude of supersymmetric particle production and decay processes. The limits on gluino and squark pair production at the LHC are particularly heavily constrained, reaching 2 TeV in many cases. With the large integrated luminosity available through the full Run 2 dataset, and the improved analysis techniques and strategies developed over the last years, the typically weaker limits on electroweakinos and sleptons are also significantly increasing and, in some cases, approach the 1 TeV mark (cf. fig. A.11 and Refs. [88, 256]). The diverse SUSY search programs at ATLAS and CMS thus increasingly constrain the existence of SUSY at the TeV scale at the LHC. Still, a number of arguments can be made that discarding the possibility for SUSY to exist at the energies available with the LHC is much too early. By the end of the lifetime of the LHC, including the HL-LHC, a











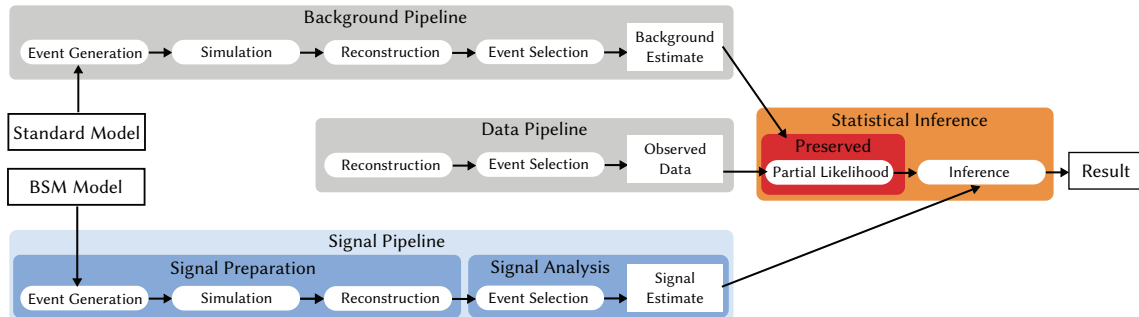


**Figure 9.1:** Full analysis workflow including the three main processing pipelines for deriving background and signal estimates as well as observed data counts. The outputs of the three processing pipelines are combined into a likelihood forming the basis for the statistical inference. In a RECAST setup (details in the text), the estimated background rates and observed data counts are archived, and the signal pipeline is fully preserved, such that it can be re-executed with different inputs at any time. Figure created by the author but based on Ref. [259].

after the expected and observed event rates in all regions are known, the statistical evaluation can be performed, and the final analysis results, e.g., quantifying excesses in data or setting limits on model parameters, can be determined. Figure 9.1 illustrates the formal structure of such an analysis, consisting of three main processing pipelines; a *background pipeline*, a *signal pipeline* and a *data pipeline*; followed by the *statistical inference*.

Due to the substantial amount of resources necessary for developing and performing an analysis, it is not feasible to develop dedicated searches for every possible BSM scenario. Instead, analyses are typically only interpreted in a finite set of models with a small number of free parameters that need to be varied. Still, it is likely that a given analysis is sensitive to a variety of different BSM scenarios not considered in the original publication. Consequently, it is not surprising that there is significant interest in the HEP community to reinterpret BSM searches in different signal models. Reinterpretations of ATLAS searches for SUSY are routinely performed by various reinterpretation efforts. In the context of direct constraints on BSM physics<sup>†</sup>, the search results published by the experimental collaborations represent the only windows into the LHC data that are available to the wider HEP community. Reinterpretations of BSM searches are thus the only possibility to determine the direct implications of LHC data for a broad range of models [258].

As will be discussed in detail in chapter 11, reinterpretations are not only of interest for the wider HEP community, but also for the experimental collaborations themselves. Within the ATLAS Collaboration, reinterpretations of SUSY searches in complete SUSY models can, for example, serve as powerful tools to state a comprehensive summary of the overall sensitivity to more realistic supersymmetric models. As such, the efforts discussed in the remainder of this chapter, as well as in chapters 10 and 11, are not only relevant for the work presented in this thesis, but also reinterpretation efforts currently ongoing within the ATLAS Collaboration.

<sup>†</sup> As discussed to some extent in section 1.2.1, indirect constraints on BSM models can also come from SM precision measurements.













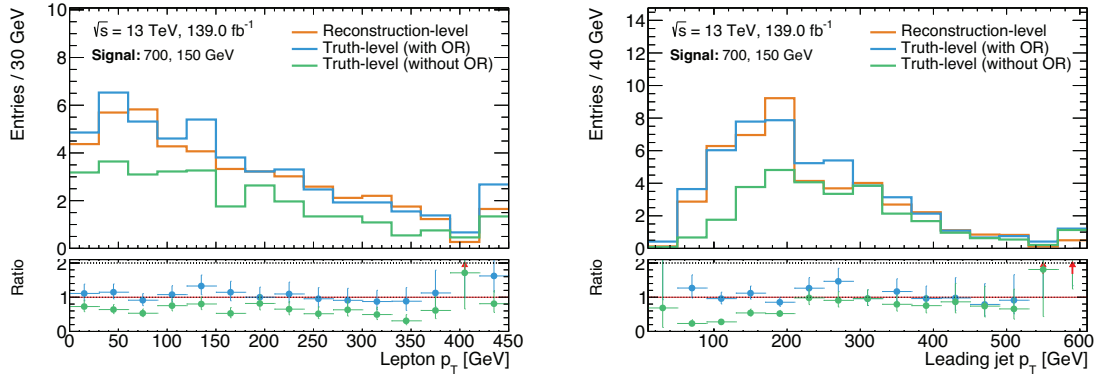


**Figure 9.3:** Impact of the overlap removal (OR) procedure at truth-level illustrated in the lepton and leading jet transverse momenta distributions. The truth-distributions with (blue) and without (green) overlap removal are compared with a reconstruction-level (orange) distribution. The exemplary benchmark signal point with  $m(\tilde{\chi}_1^\pm/\tilde{\chi}_2^0)$ ,  $m(\tilde{\chi}_1^0) = 700, 150$  GeV is shown in both plots. Both truth-level distributions are shown after smearing. All distributions are shown in a loose preselection requiring an electron or a muon,  $E_T^{\text{miss}} > 50$  GeV,  $m_T > 50$  GeV, and 2–3 jets, two of which need to be  $b$ -tagged.

as a function of said object definitions and hence still allows to consider them to some extent. Additionally, as discussed in section 9.1, the full specification of the original analysis event selection, including all object definitions, allows for more straightforward reinterpretations by efforts outside of the ATLAS Collaboration that generally do not have access to the original analysis software.

Following the object definitions, an overlap removal procedure, adhering to the same prescription for the reconstruction-level<sup>†</sup> analysis (cf. section 4.5), is performed. The truth-level overlap removal especially also relies on the same shrinking cone definitions used at reconstruction-level. Since tracking information is not available at truth-level, the overlap removal step removing electrons sharing a track with a muon is approximated by using a distance parameter of  $\Delta R = 0.01$  between the objects. Although often neglected<sup>§</sup> in reinterpretation efforts outside of the collaboration, the correct implementation of the overlap removal procedure employed in the original analysis is crucial to reproduce the signal estimates of the original analysis. Figure 9.3 illustrates this by showing the lepton and leading jet  $p_T$  distributions of an exemplary signal point in configurations with and without overlap removal at truth-level, and comparing it with the distributions obtained at reconstruction-level. Not implementing the overlap removal procedure of the original  $1\ell$  search, results in many truth-level events not passing the analysis selections. This is due to additional truth-level objects in the final state that would otherwise have been removed through the overlap removal.

Finally, the exact implementation of all analysis observables is explicitly given, followed by the definition of all control and signal regions.

<sup>†</sup> The term *reconstruction-level* here refers to distributions obtained with MC simulated datasets for which either the full detector simulation using GEANT4, or the ATLFast-II fast simulation have been run with subsequent object reconstruction.

<sup>§</sup> The overlap removal procedures in ATLAS SUSY searches tend to be quite intricate, rendering them non-trivial to re-implement without ATLAS and analysis-specific knowledge.





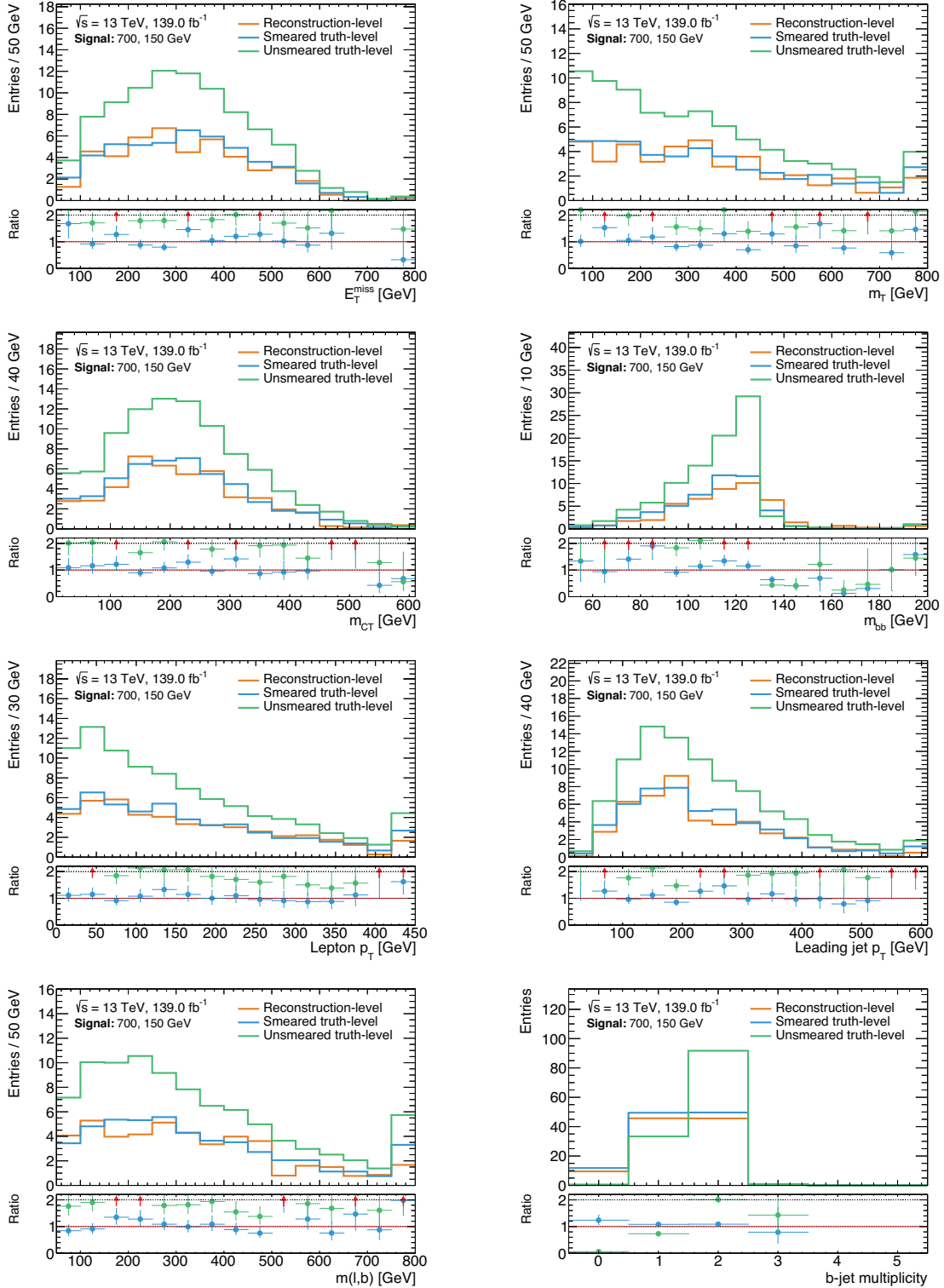


**Figure 9.4:** Comparisons of the kinematic distributions of relevant observables at (smeared) truth- and reconstruction-level. An exemplary benchmark signal point with electroweakino mass parameters  $m(\tilde{\chi}_1^\pm/\tilde{\chi}_2^0), m(\tilde{\chi}_1^0) = 700, 150 \text{ GeV}$  is shown. The ratio pad shows the ratio of smeared and unsmeared truth-level distributions (blue and green) to reconstruction-level distributions (orange). Only MC statistical uncertainties are included in the error bars. All distributions are shown in a loose preselection requiring exactly one electron or muon,  $E_T^{\text{miss}} > 50 \text{ GeV}$ ,  $m_T > 50 \text{ GeV}$ , and 2–3 jets, two of which need to be  $b$ -tagged. The latter requirement is dropped for the  $b$ -jet multiplicity distribution.



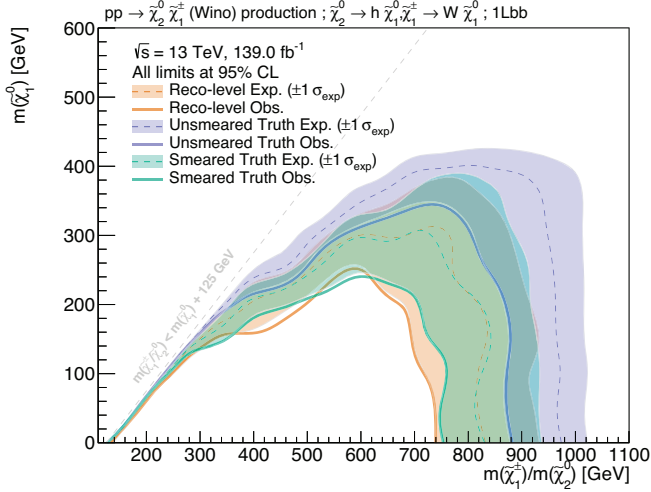


**Figure 9.6:** Expected and observed exclusion contours obtained with the full likelihood using reconstruction-level inputs (orange) as well as truth-level inputs before (purple) and after (green) smearing. Uncertainties include all statistical and systematic uncertainties on the background and signal for the reconstruction-level contours, but only statistical and systematic uncertainties on the background for truth-level signal inputs.

### 9.5.3 Validation using the likelihood

Using the nominal expected event rates at (smeared) truth-level for every signal model in the original signal grid considered in the  $1\ell$  search, expected and observed  $\text{CL}_s$  values can be computed and exclusion contours can be derived. Figure 9.6 compares the expected and observed exclusion contours obtained using the full likelihood and reconstruction-level signal inputs with those obtained using the full likelihood and truth-level signal inputs before and after truth smearing. While all systematic uncertainties on the signal are included in the reconstruction-level contours, no signal uncertainties are considered when obtaining both the smeared and unsmeared truth-level contours. The full treatment of the systematic uncertainties on the background estimates is performed in both cases. As expected from the previous validation steps in the signal regions, the sensitivity using unsmeared truth-level signal inputs is significantly overestimated compared to the published analysis exclusion limit using reconstruction-level inputs. The smeared truth-level inputs, however, yield exclusion contours with an acceptable match compared to the reconstruction-level results.

In summary, the above validation process, performed at multiple selection levels of the analysis, shows that the truth-level analysis with dedicated smearing functions yields a reasonable approximation of the signal pipeline. For signal models producing final states with kinematics close to those of the scenarios validated in the previous sections, this approach allows to determine the event rate estimates with high computational efficiency. In large-scale reinterpretations, the smeared truth-level analysis can be used as a basis for an efficient classification of models into two categories: models that are safely excluded (or not excluded) based on truth-level analysis only, and models where (non-)exclusion is in doubt and instead the precision of the full analysis pipeline using RECAST is required.



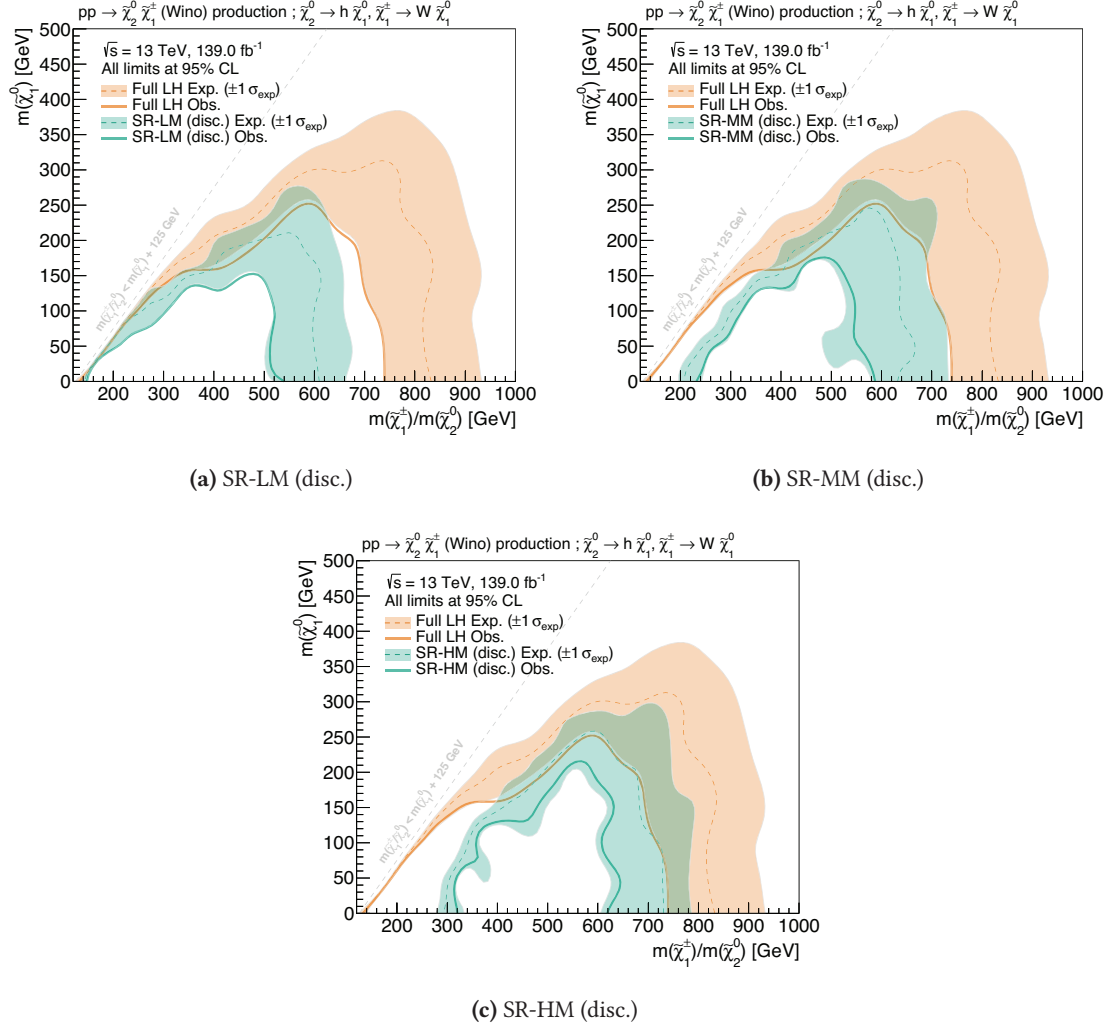


**Figure 10.1:** Comparison of exclusion limits obtained using the likelihood built from all nine exclusion signal regions (orange), and the discovery signal regions (green). As discussed in section 5.3, the discovery signal regions are simple *cut-and-count* regions making minimal model assumptions. They are not mutually exclusive and, therefore, cannot be statistically combined, resulting in three separate exclusion contours. The full set of statistical and systematic uncertainties on the background and the signal event rates are included in all regions. The shorthand notation ‘LH’ refers to likelihood.







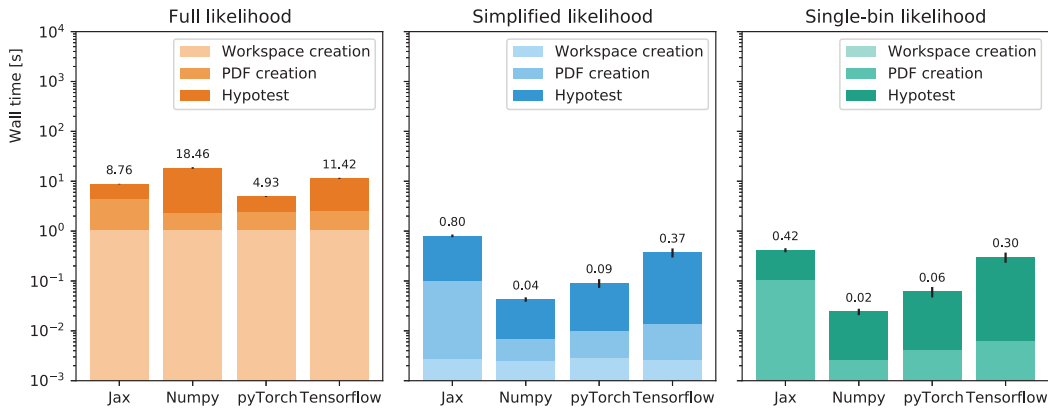


**Figure 10.2:** Benchmarks of the wall times for hypothesis testing using different likelihoods and pyhf backends in the context of the  $1\ell$  search. Benchmarking details are given in the text. The full likelihood (left) includes the full statistical implementation of the original analysis, the simplified likelihood (center) represents the simplified likelihood approach presented in this document, and the single-bin likelihood (right) represents the single-bin approximation using the discovery signal regions. The ‘workspace creation’ refers to I/O operations reading in the JSON file containing the likelihood. The ‘pdf creation’ step refers to the creation of the statistical model in a pyhf-internal structure. ‘Hypotest’ refers to the wall time of a single exclusion hypothesis test computing a  $CL_s$  value. The error bars correspond to the standard deviation of the benchmark sample.

considering the full treatment of the systematic uncertainties. The simplified likelihood approach therefore assumes the total background estimate to be fixed at the post-fit values obtained from the initial full likelihood fit, and, furthermore, only allows the background estimates to vary within the total uncertainty.

All simplified likelihoods used in the following have been produced using SIMPLIFY [285], a python tool written by the author. The background model of the simplified likelihood of the  $1\ell$  search in JSON format is available at Ref. [286]. By the means of JSON patches [287], any signal model, for which the nominal expected event rates in the analysis regions are known, can then be evaluated using this simplified likelihood.

### 10.3 Computational performance

One of the main figures of merit of an analysis approximation obviously is the reduction in computational wall time compared to the full analysis. Figure 10.2 shows the results of a benchmark for different likelihood configurations in the context of the  $1\ell$  search. The wall times of hypothesis tests using the full analysis likelihood are compared with those using the simplified likelihood constructed following the previously introduced prescription. In addition, the wall time of the single-bin likelihood relying on the discovery SRs, already used in fig. 10.1, is shown. For each likelihood, different computational backends are exploited for the tensor algebra operations in pyhf. All benchmarks have been performed on an Intel i7-4790 CPU with a nominal clock speed of 3.60 GHz, 4 cores and 8 threads. The CPU was not isolated, but under minimal load. The original 125 signal points of the  $1\ell$  search were used in each configuration.



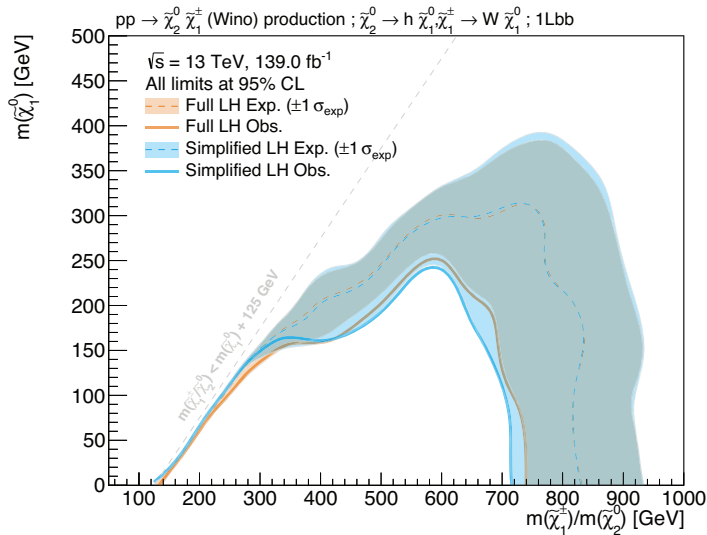


**Figure 10.3:** Comparison of the exclusion contours obtained with the simplified likelihood (blue) and the full likelihood (orange) of the  $1\ell$  search. The uncertainty band includes all MC statistical and systematic uncertainties in the case of the full likelihood, and only the simplified uncertainties in the case of the simplified likelihood. The shorthand notation ‘*LH*’ refers to likelihood.

are shown in blue, while the results obtained using the full likelihood are given in orange. Both the observed (without the usual theoretical up and down variations on the signal cross section) and expected exclusion limits including the uncertainty band are shown. In the case of the full likelihood, the complete set of MC statistical and systematic uncertainties, introduced in chapter 7, are taken into account. As discussed in section 10.2, the uncertainty band on the simplified likelihood contour results from the single nuisance parameter, built through reduction of the original nuisance parameters.

The observed and expected  $CL_s$  values, obtained using both likelihoods, are shown in fig. 10.4. As expected from the exclusion contour, both the simplified and the full likelihood agree reasonably well across the majority of the  $CL_s$  range. For signal models well within exclusion (i.e.  $CL_s \ll 0.05$ ) according to the full likelihood, the simplified likelihood of the  $1\ell$  search tends to result in slightly lower  $CL_s$  values, yielding a slightly too optimistic sensitivity estimate. In the range relevant to the exclusion contour at 95% CL (i.e.  $CL_s \approx 0.05$ ), the results from the simplified likelihood agree well with those from the full likelihood.

In addition to the  $1\ell$  search, the simplified likelihood approach has been validated on the ATLAS searches for SUSY listed in table 10.1. An overview of the results is shown in fig. 10.5, comparing the exclusion contours obtained with the simplified likelihood against the full analysis results. In some analyses, e.g., the ATLAS sbottom and ATLAS  $3\ell$  searches, both likelihoods are in excellent agreement. In other analyses, like e.g., the ATLAS direct stau search, the agreement is less impressive but overall still acceptable.

In summary, this validation demonstrates that the simplified likelihood method introduced herein can, in many cases, offer a computationally efficient and reliable approximation of ATLAS searches for SUSY relying on the HISTFACTORY pdf template.

## 10.5 Limitations

Building a well-performing simplified likelihood is not always as straightforward as described in section 10.2, and some analyses require special care when being approximated. For example, in

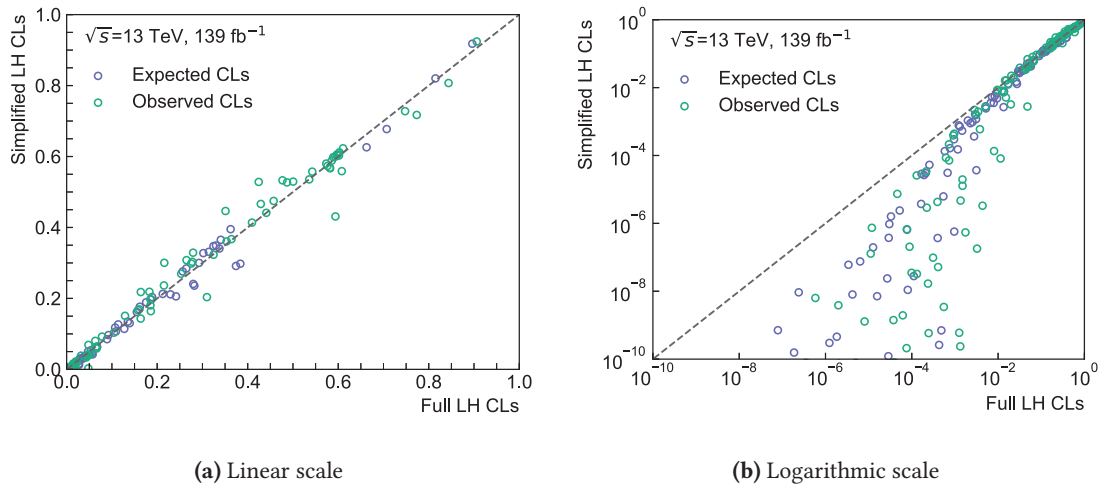


**Figure 10.4:** Scatter plots comparing the observed and expected  $CL_s$  values obtained using the simplified and the full likelihoods for the same set of signal models considered in the  $1\ell$  search. Both linear and logarithmic scale representations are shown to give an overview of the full range of  $CL_s$  values.

the case of the ATLAS compressed search [91], shown in fig. 10.5(f), only a subset of the original analysis signal regions are entering the simplified likelihood. Studies have shown this to result in an overall improvement in agreement between the two likelihoods. The straightforward structure of the simplified likelihood is, in this case, not able to reproduce the statistical behaviour of the background model of the full likelihood in the signal regions omitted. As these signal regions were found to only add limited sensitivity to the search, their removal in the simplified likelihood yields an overall improvement in agreement. Figure B.4 further illustrates the impact of removing these signal regions in the simplified likelihood.

It is worth highlighting again that the simplified likelihood assumes the total background model to be describable by a single sample with a single rate modifier, constrained by a Gaussian and correlated over all bins, with background event rates and uncertainties obtained from a background-only fit using the full likelihood. This, in particular, assumes that the background model is sufficiently constrained by the large statistics in the CRs and that the introduction of signal contributions—especially in the SRs—does not significantly change the background model in a way that cannot be replicated with the simplified likelihood. A configuration, where the background model is no longer mostly constrained by the large statistics in the control regions is tolerable to some extent in the full analysis likelihood, but turns out to be problematic for the simplified likelihood, as it lacks the number of parameters to be able to replicate the behaviour of the full likelihood.

An additional limitation arises in cases of significant signal contamination in the CRs. In the full likelihood, significant signal contaminations in the CRs generally lead to smaller background estimates in the SRs, which, in turn, result in conservative exclusion limits given the observed data. In the simplified likelihood, even with the CRs included, the single constrained nuisance parameter does not offer enough degrees of freedom<sup>†</sup> to scale down the background model in

<sup>†</sup> In the full likelihood the normalisation of the SM background is taken care of through floating normalisation parameters (and to some extent other constrained parameters), hence there are more degrees of freedom to fit the model to data.

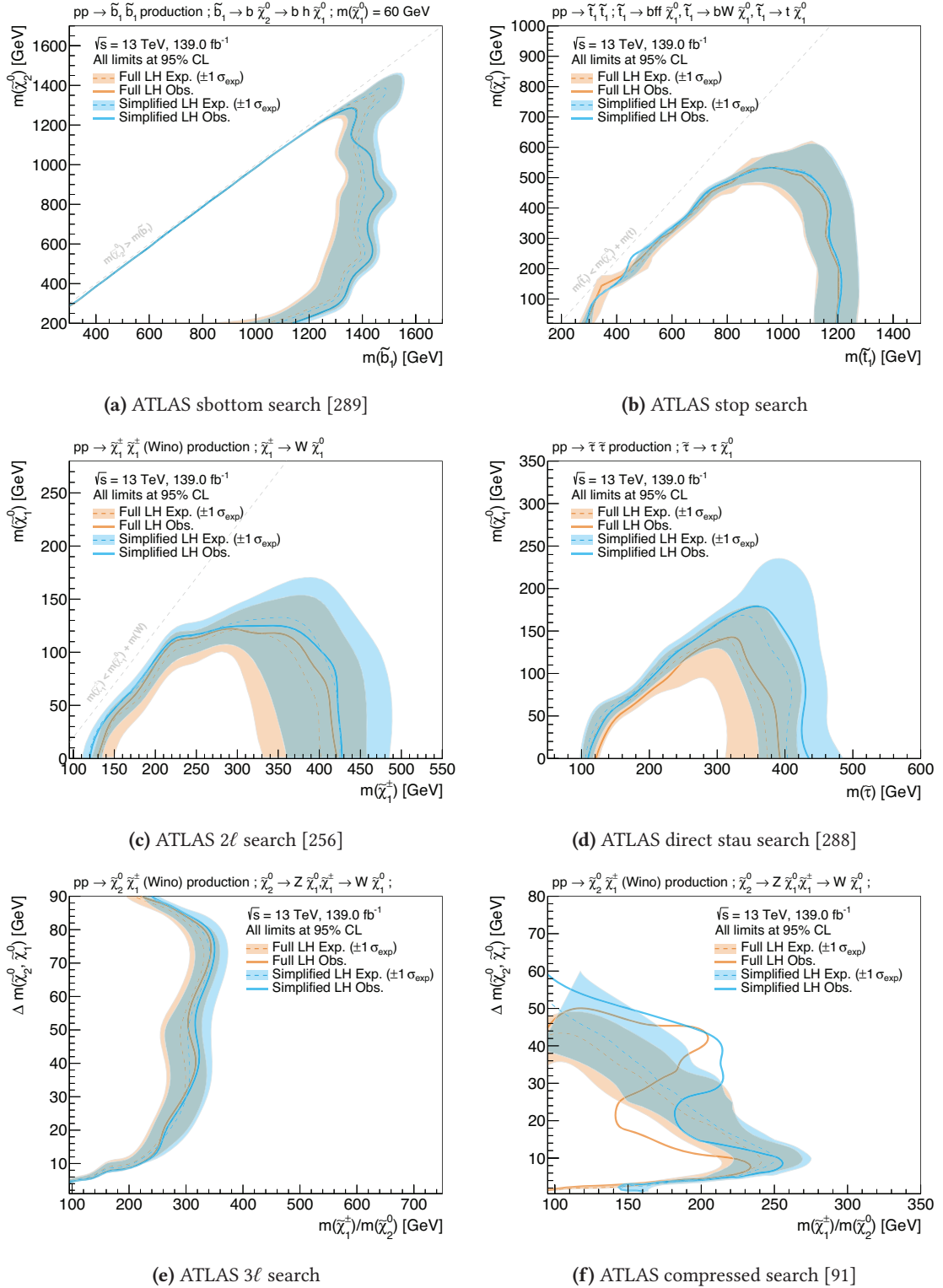


**Figure 10.5:** Simplified likelihood results for the different ATLAS searches studied. The results from the simplified likelihood (blue) are compared with the results of the full analysis likelihood (orange). The same reconstruction-level signal inputs are used in both cases. The shorthand notation ‘*LH*’ refers to likelihood.

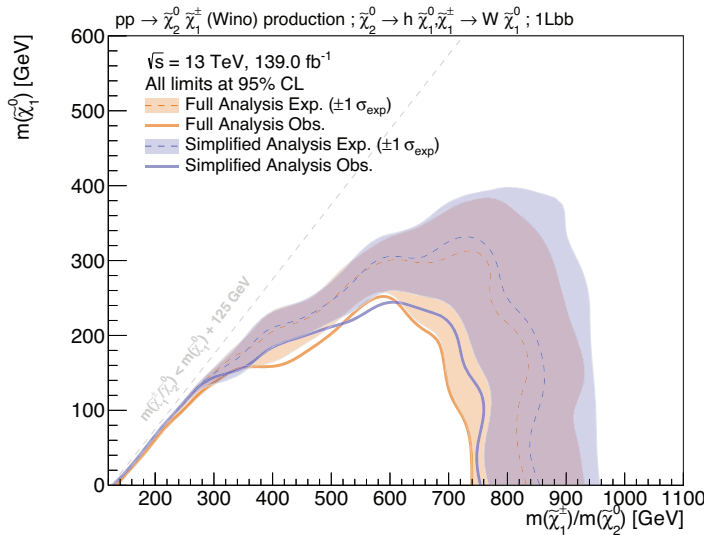


**Figure 10.6:** Expected and observed exclusion contours obtained with the full likelihood and reconstruction-level inputs (orange) and the simplified likelihood and smeared truth-level inputs (purple). All statistical and systematic uncertainties on the background and signal are considered for the reconstruction-level contours determined using the full likelihood.

the  $\mu = 1$  hypothesis to the levels obtained in the full likelihood, ultimately resulting in *fake* sensitivity in the CRs. Although it is generally important to limit signal contamination in the CRs for the sake of healthy profile likelihood fits, this is especially true in the case of very simplified likelihoods, like the one introduced herein. In the case of the ATLAS stop search, shown in fig. 10.5(b), significant signal contamination<sup>†</sup> of more than 30% appears in the control regions for many signal models with  $m(\tilde{t}_1) < m(\tilde{\chi}_1^0) + m(t)$ , thereby breaking one of the base assumptions of the simplified likelihood. In fig. B.5, the impact of applying the simplified likelihood on signal models with significant signal contamination in the region  $m(\tilde{t}_1) < m(\tilde{\chi}_1^0) + m(t)$  is shown. In practice, this means that models need to be carefully checked for potential signal contamination in the control regions, and cannot be evaluated using the simplified likelihood in case the signal contamination is found to be too high<sup>§</sup>.

## 10.6 Outlook and future prospects

The simplified likelihood method [284] introduced in this chapter can offer precise and computationally efficient approximations of ATLAS SUSY searches for which the full likelihood in JSON format is available. A publicly available python tool has been developed for the generic conversion of any full likelihood in JSON format into the simplified format introduced herein [285].

The procedure of approximating the statistical model of a search is orthogonal to the truth-level analysis discussed in section 9.4 in the sense that both approximations target a different part of the analysis workflow shown in fig. 9.1. As such, both approaches can be combined into a *simplified analysis* that runs a smeared truth-level analysis in order to determine an estimate for the signal event rates, followed by a simplified statistical inference using the simplified likelihood. Figure 10.6 compares the expected and observed exclusion contours obtained in the full  $1\ell$  search with those

<sup>†</sup> Since the kinematic properties of the  $\tilde{t}_1$  decays drastically change in the parameter region with  $m(\tilde{t}_1) < m(\tilde{\chi}_1^0) + m(t)$ , this is a kinematic region that the analysis is not designed to be sensitive to. Therefore the CRs are not guaranteed to be free of signal contamination.

<sup>§</sup> The exact amount of tolerable signal contamination should be explicitly checked on a per-analysis basis. For models exceeding the tolerated amount, the full likelihood may be used instead of the simplified one.









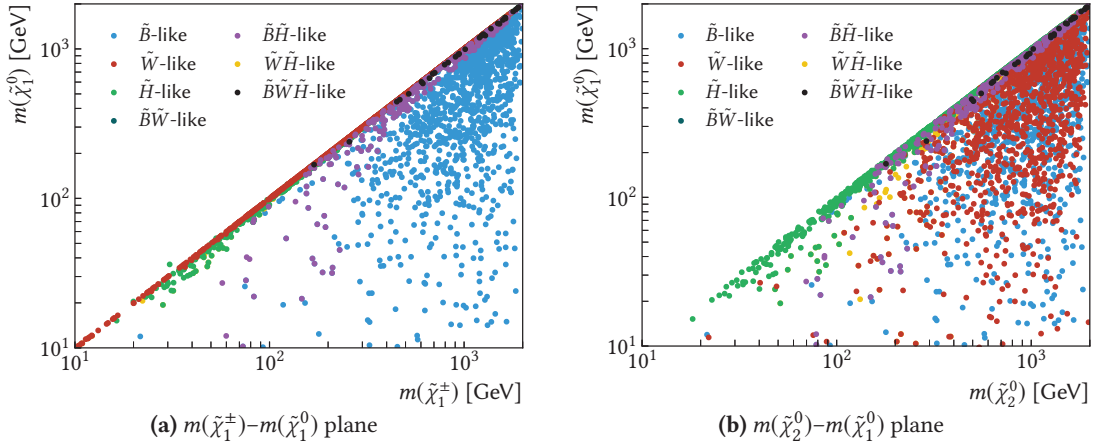


**Figure 11.1:** Projections of all models sampled onto the (a)  $m(\tilde{\chi}_1^\pm) - m(\tilde{\chi}_1^0)$  and (b)  $m(\tilde{\chi}_2^0) - m(\tilde{\chi}_1^0)$  planes. Each point represents a distinct pMSSM model with a unique combination of pMSSM parameters. The colour encodes the composition of the  $\tilde{\chi}_1^0$  in each model. Details on how the LSP type is defined are given in the text.

#### 11.2.4 Truth-level analysis

All models passing event generation are evaluated using the simplified analysis comprised of truth-level inputs, four-vector smearing and the simplified likelihood. This is the only evaluation done for the models considered herein. A full scan over the pMSSM including multiple ATLAS searches would additionally include a processing step reverting back to the full analysis available through RECAST for model points where (non-)exclusion is uncertain based on the simplified analysis only.

### 11.3 Phenomenology of the LSP

The composition of the  $\tilde{\chi}_1^0$  in each pMSSM model sampled is shown in projections onto the  $m(\tilde{\chi}_1^\pm) - m(\tilde{\chi}_1^0)$  and  $m(\tilde{\chi}_2^0) - m(\tilde{\chi}_1^0)$  planes in figs. 11.1(a) and 11.1(b), respectively. The  $\tilde{\chi}_1^0$  is considered to be bino-like ( $\tilde{B}$ -like), wino-like ( $\tilde{W}$ -like) or higgsino-like ( $\tilde{H}$ -like) if the corresponding fraction from the neutralino mass mixing matrix is at least 80%. If more than one component has a fraction of more than 20%, then the  $\tilde{\chi}_1^0$  is considered to be of mixed nature. For example, a  $\tilde{\chi}_1^0$  with more than 20% bino-, wino- and higgsino-components is referred to as  $\tilde{B}\tilde{W}\tilde{H}$ -like. The nature of the LSP as a function of the bino, wino and higgsino mass parameters ( $M_1$ ,  $M_2$  and  $\mu$ ) is shown as a reference in fig. C.2.

In the bulk of the  $m(\tilde{\chi}_1^\pm) - m(\tilde{\chi}_1^0)$  plane, i.e. the parameter space targeted by the  $1\ell$  search using the simplified model, a large majority of the models produce a bino-like LSP with nearly mass-degenerate  $\tilde{\chi}_1^\pm$  and  $\tilde{\chi}_2^0$ . These models correspond to cases where  $M_1 \ll \mu$  and  $M_1 < M_2$  and thus produce electroweakino spectra similar to the canonical simplified model considered in the  $1\ell$  search. Some sensitivity can therefore be expected towards these models in the context of the  $1\ell$  search, provided that the decays  $\tilde{\chi}_1^\pm \rightarrow W^\pm \tilde{\chi}_1^0$  and  $\tilde{\chi}_2^0 \rightarrow h \tilde{\chi}_1^0$  have sufficiently large branching fractions and produce on-shell bosons.





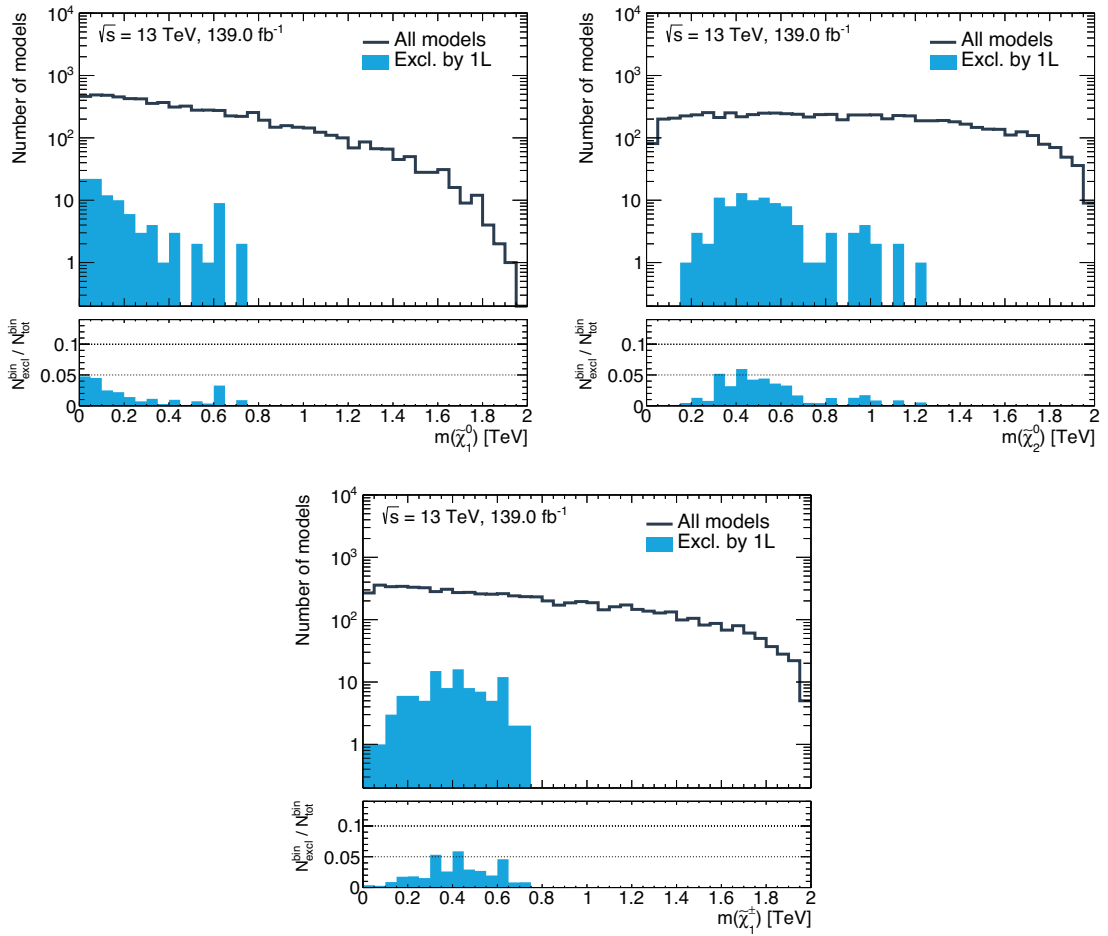


**Figure 11.3:** Bin-by-bin number of excluded models as a one-dimensional function of the electroweakino masses. The bin-wise fraction of excluded models,  $N_{\text{excl}}^{\text{bin}} / N_{\text{tot}}^{\text{bin}}$ , is shown in the lower pad. All models are evaluated using the simplified likelihood of the  $1\ell$  search.



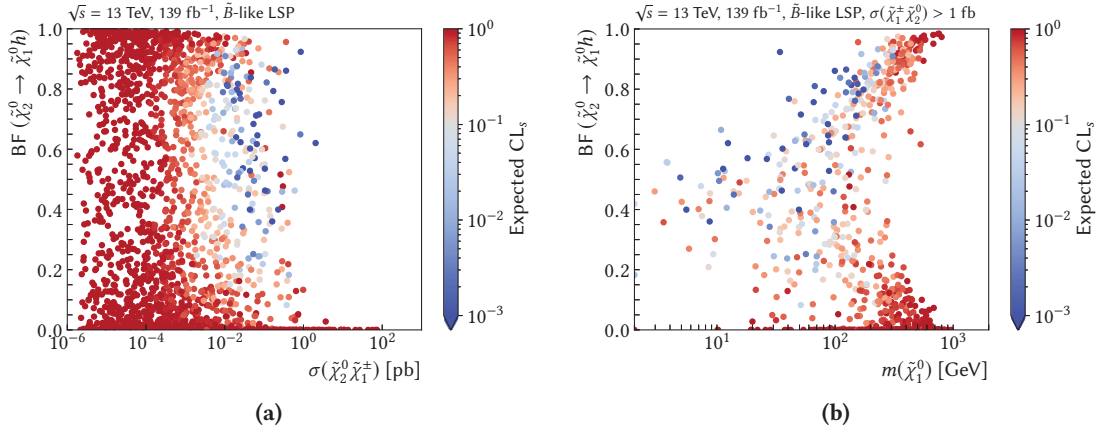


**Figure 11.5:** Density of the pMSSM models with bino-like  $\tilde{\chi}_1^0$  projected onto the plane spanned by (a) the  $\tilde{\chi}_1^\pm \tilde{\chi}_2^0$  pair production cross section and  $BF(\tilde{\chi}_2^0 \rightarrow h\tilde{\chi}_1^0)$ , and (b)  $m(\tilde{\chi}_1^0)$  and  $BF(\tilde{\chi}_2^0 \rightarrow h\tilde{\chi}_1^0)$ . The expected  $CL_s$  value obtained for each model using the  $1\ell$  search is colour-encoded. While models with a red tint are not expected to be excluded, models with a neutral white tint are on the boundary of expected exclusion, and models with a blue tint are expected to be excluded. Only models with a bino-like LSP are shown in both figures. In fig. (b), models are also required to satisfy  $\sigma(\tilde{\chi}_1^\pm \tilde{\chi}_2^0) > 1 \text{ fb}$ .

model contour. The loss in sensitivity can be attributed to the fact that the simplified model assumes branching fractions of 100% of the  $\tilde{\chi}_1^\pm \rightarrow W^\pm \tilde{\chi}_1^0$  and  $\tilde{\chi}_2^0 \rightarrow h\tilde{\chi}_1^0$  decays (with on-shell  $W$  and  $h$  bosons). The decay of the chargino through an on-shell  $W$  boson is, in general, a good assumption in  $R$ -parity conserving models with  $m(\tilde{\chi}_1^\pm) \gtrsim m(\tilde{\chi}_1^0) + m(W)$  and where the sleptons and charged and pseudoscalar Higgs bosons are heavier than the charginos and neutralinos. The decay of the next-to-lightest neutralino through a Higgs boson, however, turns out not to be the most probable decay mode in many models where the competing decay  $\tilde{\chi}_2^0 \rightarrow Z\tilde{\chi}_1^0$  dominates instead. The couplings of the next-to-lightest neutralino to the Higgs boson are suppressed by powers of  $|\mu|/M_2$  in the gaugino-like regions [301], meaning that the branching fraction of the  $\tilde{\chi}_2^0 \rightarrow h\tilde{\chi}_1^0$  decay takes on reasonably high values only in models with an LSP containing a substantial bino component<sup>†</sup>.

In the bulk of the  $\tilde{\chi}_1^\pm - \tilde{\chi}_1^0$  plane (cf. fig. 11.2(a)) that mostly contains models with a bino-like LSP, many models cannot be excluded simply due to their relatively high  $\tilde{\chi}_1^\pm / \tilde{\chi}_2^0$  masses, and thus low  $\tilde{\chi}_1^\pm \tilde{\chi}_2^0$  pair production cross sections. Figure 11.5(a) shows a projection of the pMSSM models in a two-dimensional plane spanned by the  $\tilde{\chi}_1^\pm \tilde{\chi}_2^0$  pair production cross section and  $BF(\tilde{\chi}_2^0 \rightarrow h\tilde{\chi}_1^0)$ . The colour of each model point indicates the expected  $CL_s$  value<sup>§</sup>, revealing that the  $1\ell$  search only starts to become sensitive to models with  $\sigma(\tilde{\chi}_1^\pm \tilde{\chi}_2^0) > \mathcal{O}(1 \text{ fb})$ . This is in line with the sensitivity of the  $1\ell$  analysis obtained in the simplified model scenario, where model points with electroweakino pair production cross sections as low as  $4.1 \text{ fb}$  were expected to be excluded. Figure 11.5(a) moreover shows that, for many models with  $\sigma(\tilde{\chi}_1^\pm \tilde{\chi}_2^0) \gtrsim 1 \text{ fb}$ , the branching fraction of the next-to-lightest neutralino decay via a Higgs boson is vanishingly small. This ultimately results in a low number of events with Higgs boson candidates, causing a lack of sensitivity in the context of the  $1\ell$  search.

<sup>†</sup> The Higgs coupling suppression is illustrated in fig. C.4.

<sup>§</sup> The expected  $CL_s$  is preferred here over the observed one as it provides a better overview of the sensitivity of the  $1\ell$  search.



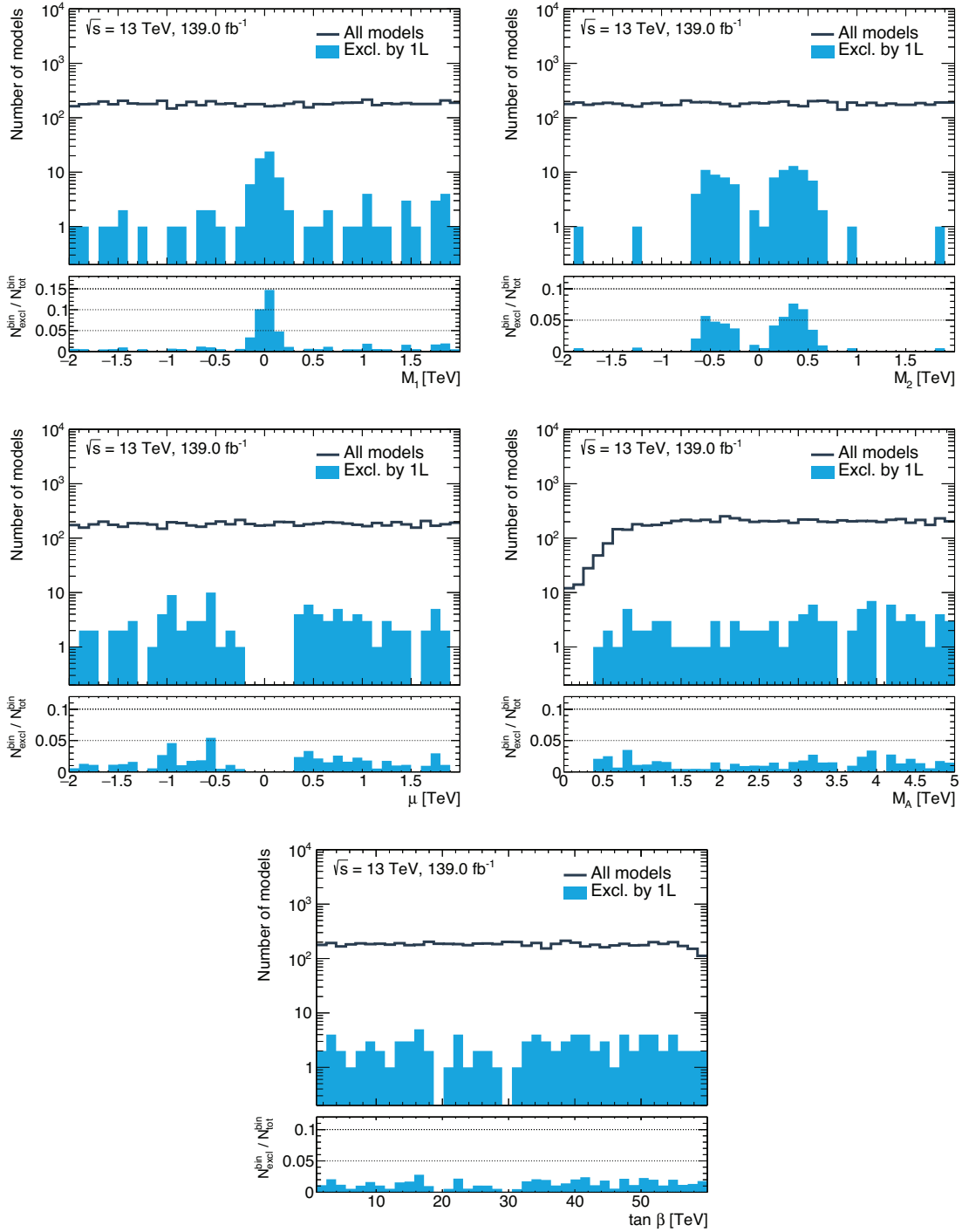


**Figure 11.7:** Bin-by-bin number of excluded models as a one-dimensional function of the pMSSM parameters relevant to the electroweak sector. The bin-wise fraction of excluded models,  $N_{\text{excl}}^{\text{bin}} / N_{\text{tot}}^{\text{bin}}$ , is shown in the lower pad. All models are evaluated using the simplified likelihood of the  $1\ell$  search.

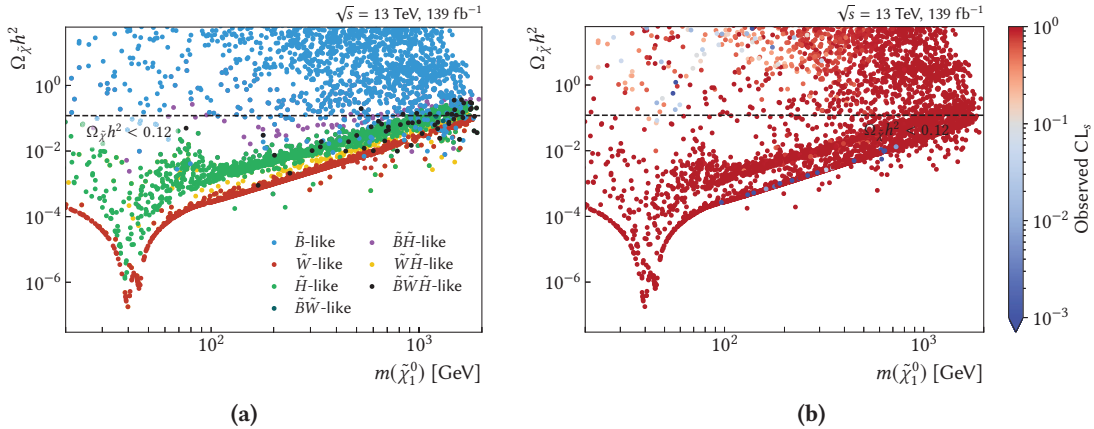


**Figure 11.8:** Density of the pMSSM model points sampled in the plane spanned by the relic density and mass of the lightest neutralino. The model points are additionally shown as a function of (a) the nature of the LSP and (b) the observed  $\text{CL}_s$  value obtained for  $139 \text{ fb}^{-1}$  of data using the  $1\ell$  search. The horizontal dashed line represents the DM relic density measurement by the Planck Collaboration [47], interpreted as an upper limit,  $\Omega_{\tilde{\chi}} h^2 < 0.12$ , such that the lightest neutralino can be a sub-dominant DM component.

of excluded models peaks at slightly higher values in the distribution of the wino mass parameter, i.e. at around  $|M_2| \approx 400 \text{ GeV}$ . As the search is not sensitive to compressed scenarios with a higgsino-like LSP, no models with small values in  $|\mu|$  can be excluded.

Since the pseudoscalar Higgs boson does not directly enter the phenomenology of the models targeted by the  $1\ell$  search, only indirect constraints can be set on  $m_A$ , excluding models across the full range of the  $m_A$  distribution sampled. A similar behaviour is observed in  $\tan \beta$  where the excluded models have values of  $\tan \beta$  spanning the full range from 1 to 60. Likewise, no direct constraints on the trilinear scalar couplings ( $A_t, A_b, A_\tau$ ), and the remaining gluino and third generation squark mass parameters ( $M_3, m_{\tilde{Q}_3}, m_{\tilde{u}_3}, m_{\tilde{d}_3}$ ) is observed<sup>†</sup>.

### 11.4.3 Impact on dark matter relic density

The cosmological abundance of the lightest neutralino  $\Omega_{\tilde{\chi}} h^2$  as a function of its type and mass is shown in fig. 11.8(a). The value of the DM relic density measured by the Planck Collaboration is also given [47]. The Planck measurement is interpreted as an upper limit on the DM relic density, thus allowing the  $\tilde{\chi}_1^0$  to be a sub-dominant DM component.

Some interesting features are worth highlighting in fig. 11.8(a). First, most of the models sampled with a bino-like  $\tilde{\chi}_1^0$  overproduce DM and result in a cosmological abundance that is too high. Of the pMSSM models sampled herein, only models with a  $\tilde{\chi}_1^0$  containing a considerable wino or higgsino component consistently satisfy  $\Omega_{\tilde{\chi}} h^2 < 0.12$  over a large range of the neutralino mass. Models with  $m(\tilde{\chi}_1^0) \simeq m(Z)/2$  can produce especially low values in  $\Omega_{\tilde{\chi}} h^2$  as the neutralino can resonantly annihilate through s-channel  $Z$  exchange. This is the so-called *Z-funnel*, a mechanism that becomes more efficient, the larger the higgsino component of the lightest neutralino is [302]. Likewise, models with a nearly mass-degenerate  $\tilde{\chi}_1^\pm \tilde{\chi}_1^0$  pair with  $m(\tilde{\chi}_1^\pm / \tilde{\chi}_2^0) \simeq m(W)/2$  can also produce low relic densities because of  $\tilde{\chi}_1^\pm \tilde{\chi}_1^0$  co-annihilation through s-channel  $W$  exchange. A

<sup>†</sup> Illustrated in fig. C.6.























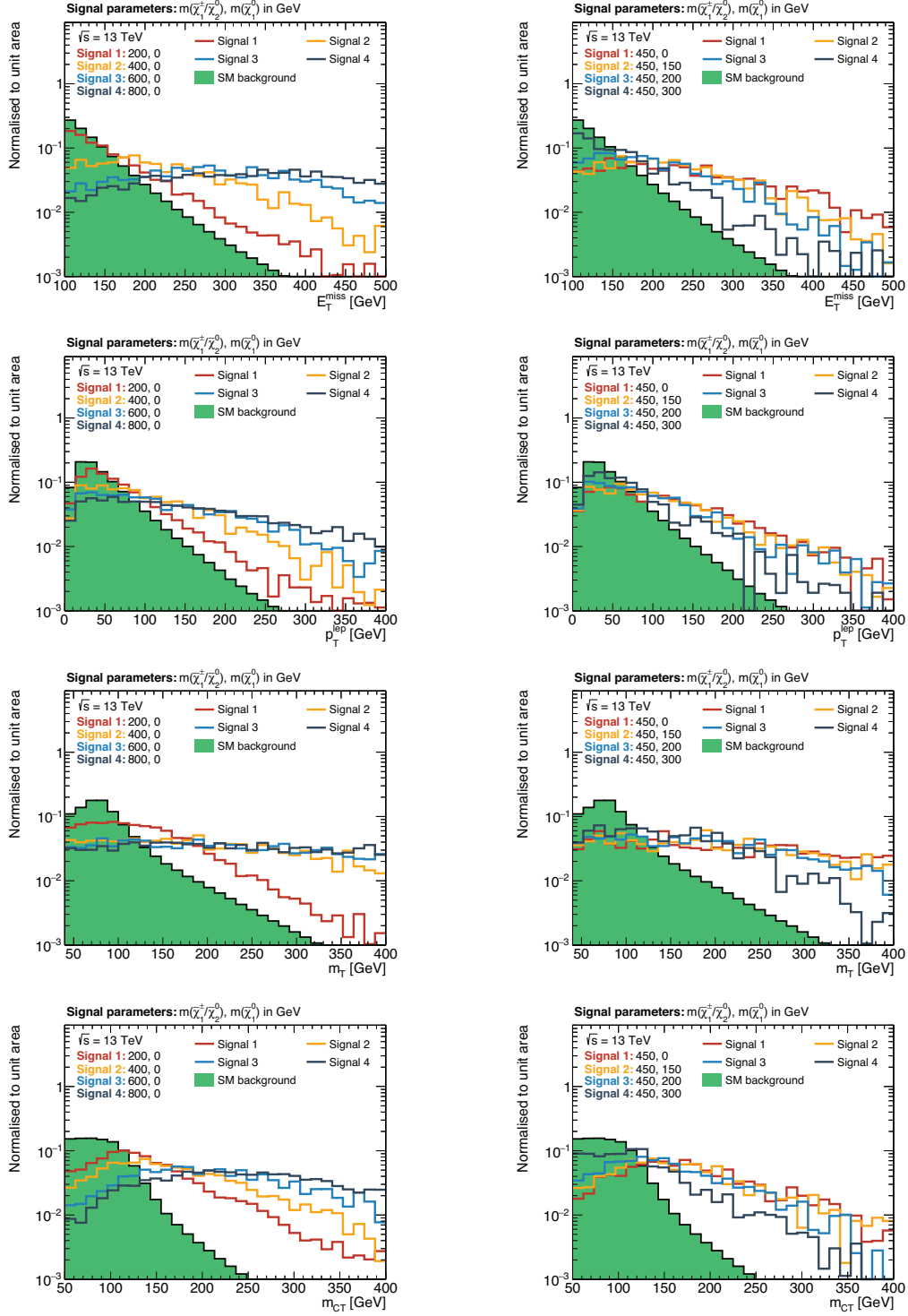


**Figure A.1:** Dependence of some of the kinematic observables on the  $\tilde{\chi}_1^\pm/\tilde{\chi}_2^0$  mass scale (left) and  $\tilde{\chi}_1^\pm/\tilde{\chi}_2^0 - \tilde{\chi}_1^0$  mass differences (right). The simulated SM backgrounds are stacked on top of each other and summarised in a single ‘SM’ histogram. Distributions from exemplary signal models with the quoted mass parameters are overlaid. In order to emphasise the shape differences, both total background and signal distributions are normalised to unity. A preselection requiring a lepton, at least two jets and  $E_T^{\text{miss}} > 100 \text{ GeV}$  is applied.

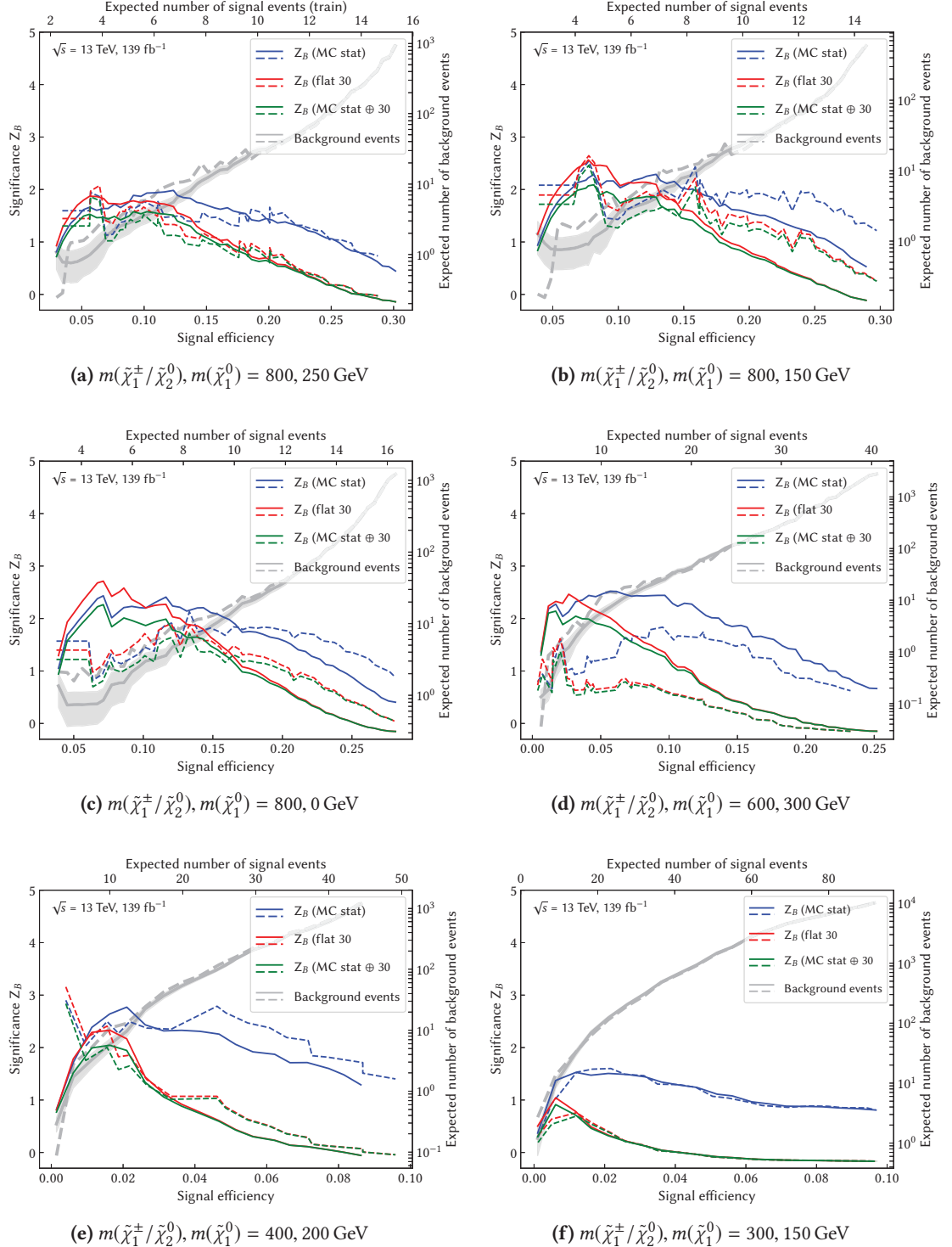


**Figure A.2:** Results of the  $N$ -dimensional cut scan for all benchmark points. The binomial discovery significance  $Z_B$  is plotted against the signal efficiency for varying uncertainty configurations. Additionally, the expected SM background rates are shown, including statistical uncertainties for one of the two statistically independent samples (shaded area). The solid and dashed lines represent the two statistically independent subsets that the MC datasets are split into.

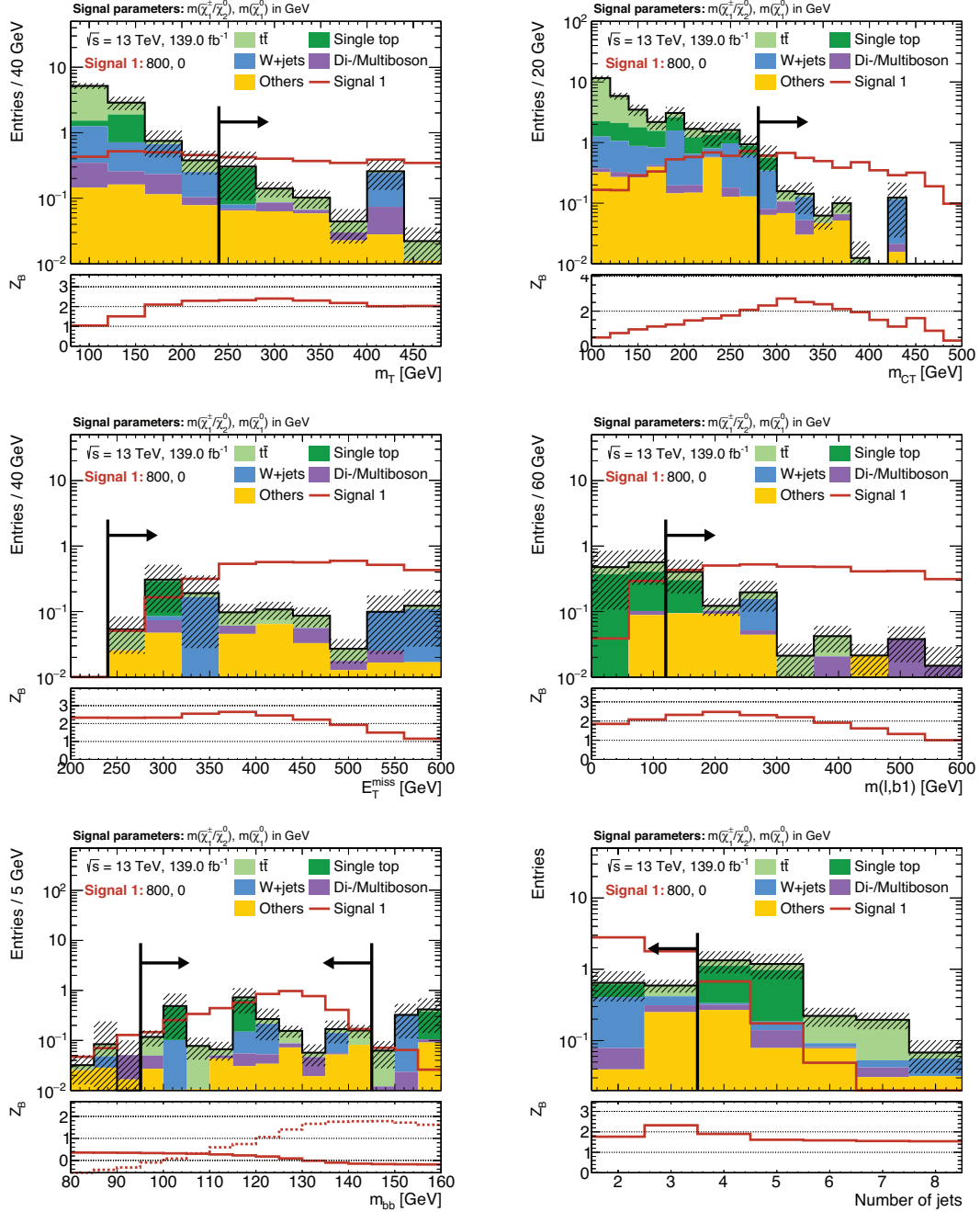


**Figure A.3:**  $N-1$  plots for the chosen cut combination for the  $(m(\tilde{\chi}_1^\pm/\tilde{\chi}_2^0), m(\tilde{\chi}_1^0)) = (800 \text{ GeV}, 0 \text{ GeV})$  signal point. The shaded region includes MC statistical as well as 30% systematic uncertainties (added in quadrature) on the background. The significance is computed using the binomial discovery significance using the uncertainty on the background.

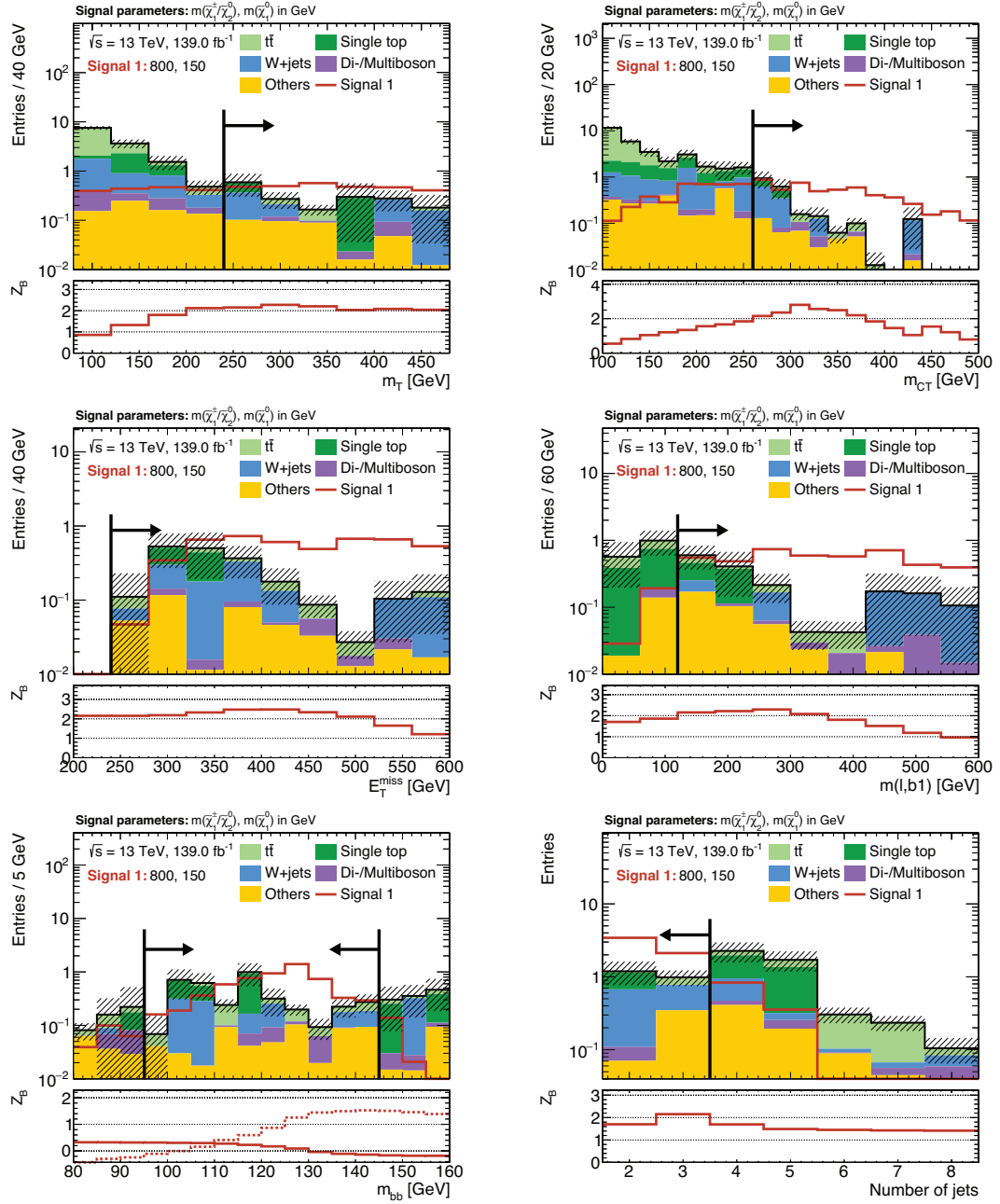


**Figure A.4:** N-1 plots for the chosen cut combination for the  $(m(\tilde{\chi}_1^\pm/\tilde{\chi}_2^0), m(\tilde{\chi}_1^0)) = (800 \text{ GeV}, 150 \text{ GeV})$  signal point. The shaded region includes MC statistical as well as 30% systematic uncertainties (added in quadrature) on the background. The significance is computed using the binomial discovery significance using the uncertainty on the background.

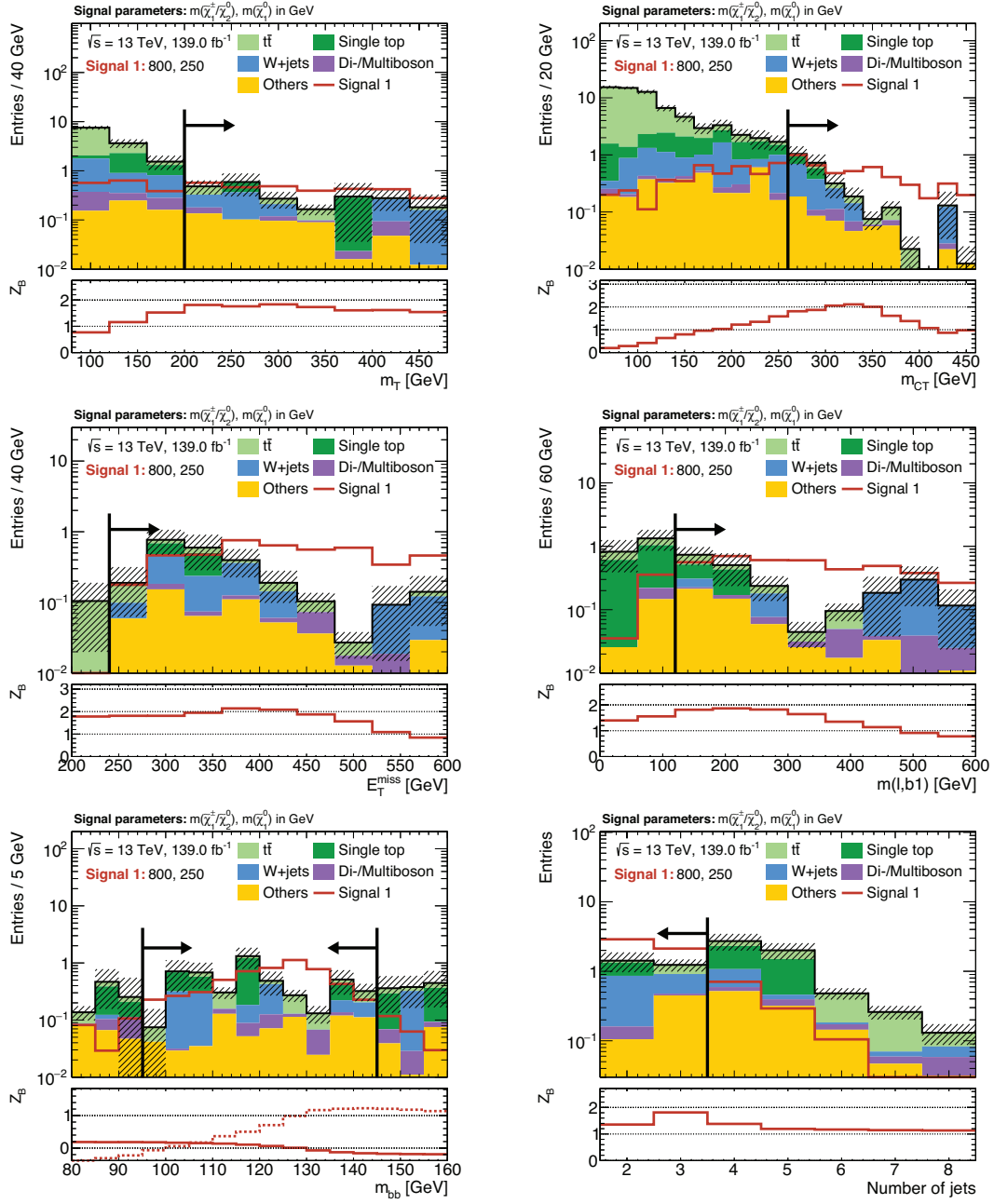


**Figure A.5:**  $N-1$  plots for the chosen cut combination for the  $(m(\tilde{\chi}_1^\pm/\tilde{\chi}_2^0), m(\tilde{\chi}_1^0)) = (800 \text{ GeV}, 250 \text{ GeV})$  signal point. The shaded region includes MC statistical as well as 30% systematic uncertainties (added in quadrature) on the background. The significance is computed using the binomial discovery significance using the uncertainty on the background.

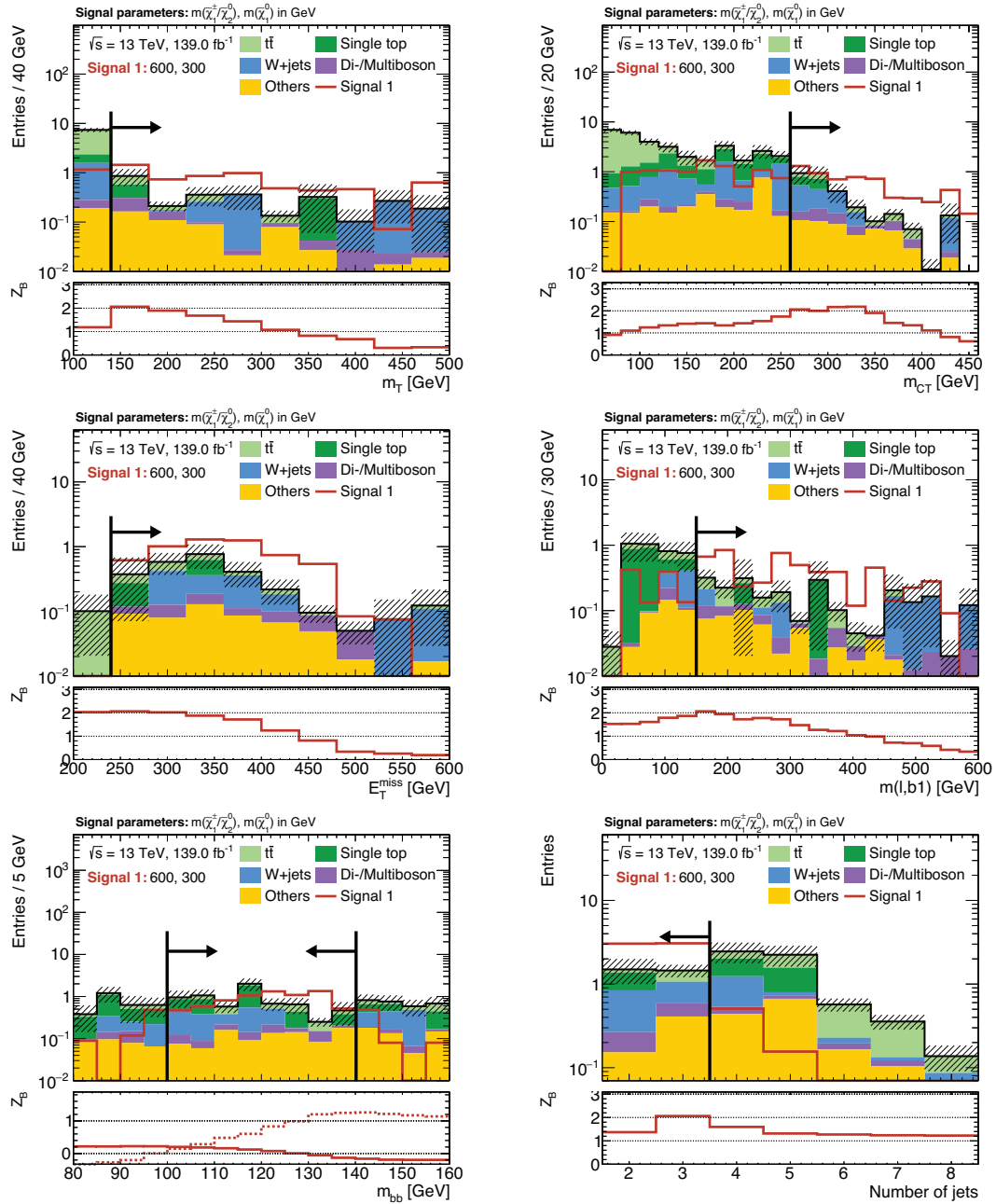


**Figure A.6:**  $N-1$  plots for the chosen cut combination for the  $(m(\tilde{\chi}_1^\pm/\tilde{\chi}_2^0), m(\tilde{\chi}_1^0)) = (600 \text{ GeV}, 300 \text{ GeV})$  signal point. The shaded region includes MC statistical as well as 30% systematic uncertainties (added in quadrature) on the background. The significance is computed using the binomial discovery significance using the uncertainty on the background.

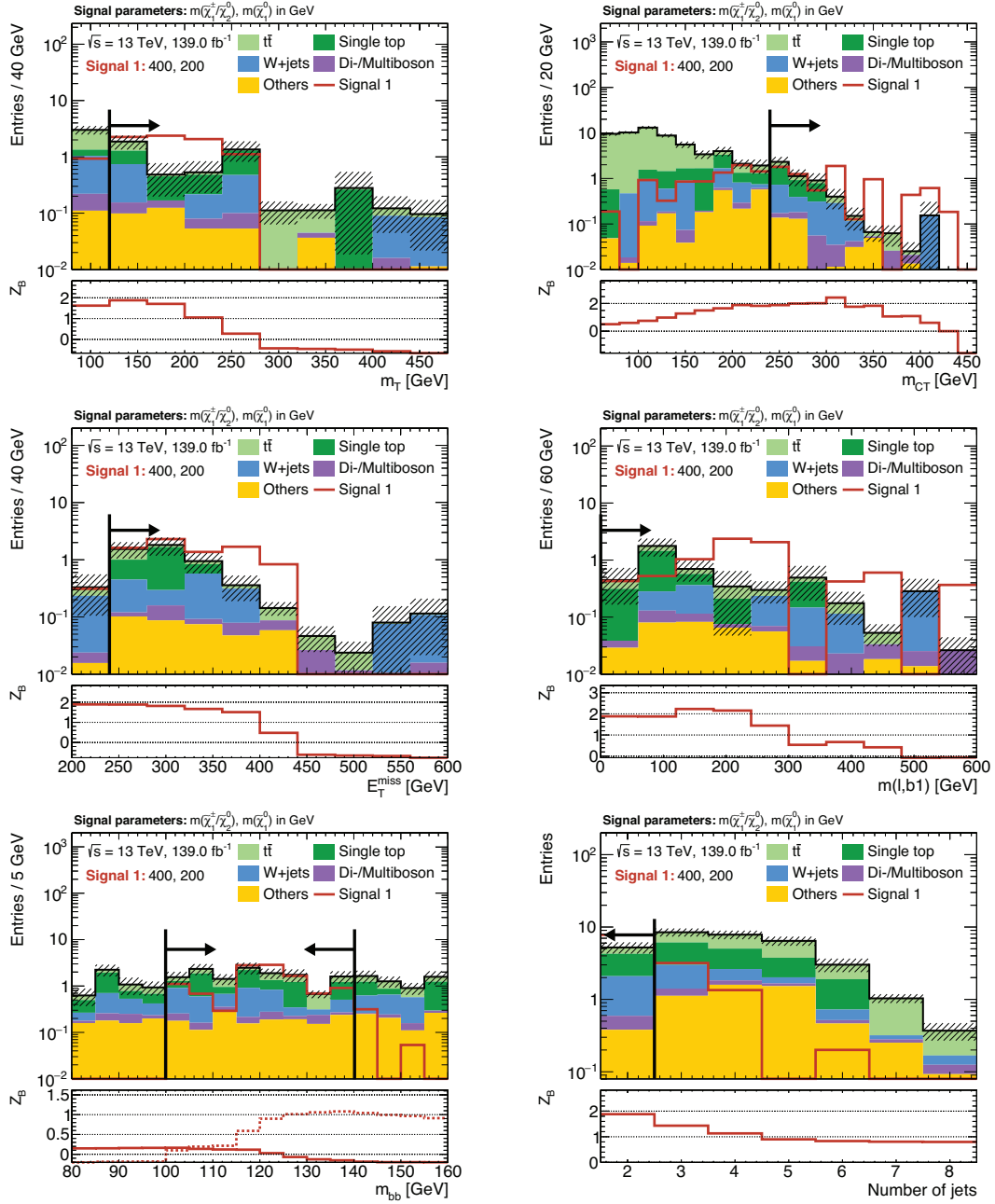


**Figure A.7:** N-1 plots for the chosen cut combination for the  $(m(\tilde{\chi}_1^\pm/\tilde{\chi}_2^0), m(\tilde{\chi}_1^0)) = (400 \text{ GeV}, 200 \text{ GeV})$  signal point. The shaded region includes MC statistical as well as 30% systematic uncertainties (added in quadrature) on the background. The significance is computed using the binomial discovery significance using the uncertainty on the background.

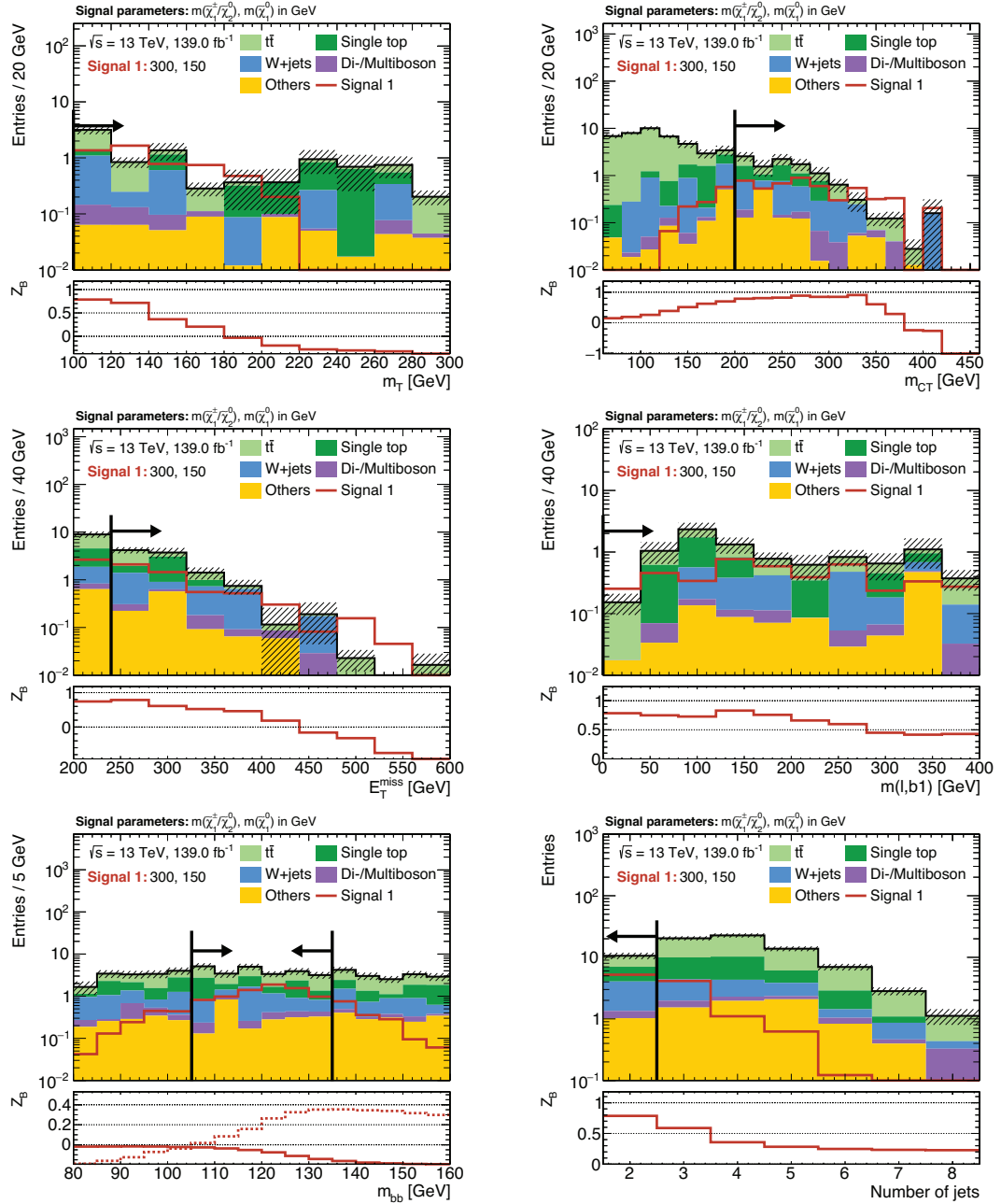


**Figure A.8:**  $N-1$  plots for the chosen cut combination for the  $(m(\tilde{\chi}_1^\pm/\tilde{\chi}_2^0), m(\tilde{\chi}_1^0)) = (300 \text{ GeV}, 150 \text{ GeV})$  signal point. The shaded region includes MC statistical as well as 30% systematic uncertainties (added in quadrature) on the background. The significance is computed using the binomial discovery significance using the uncertainty on the background.

### A.2.2 Impact of $m_{\ell b_1}$

As discussed in section 4.6, the distribution of  $m_{\ell b_1}$  has a kinematic endpoint at about 153 GeV for  $t\bar{t}$  and single top production events where the lepton and leading  $b$ -jet originate from the same top quark decay. In the SUSY processes considered,  $m_{\ell b_1}$  depends on the mass-scale of the electroweakinos pair-produced, and thus offers especially good discriminative power in the high electroweakino mass regime targeted by SR-HM.

Figure A.9 illustrates the impact of adding a requirement of  $m_{\ell b_1} > 120$  GeV in SR-HM, revealing a noticeable increase in sensitivity towards high electroweakino masses. Studies have shown that the addition of  $m_{\ell b_1} > 120$  GeV to the remaining signal regions does not improve the sensitivity further.

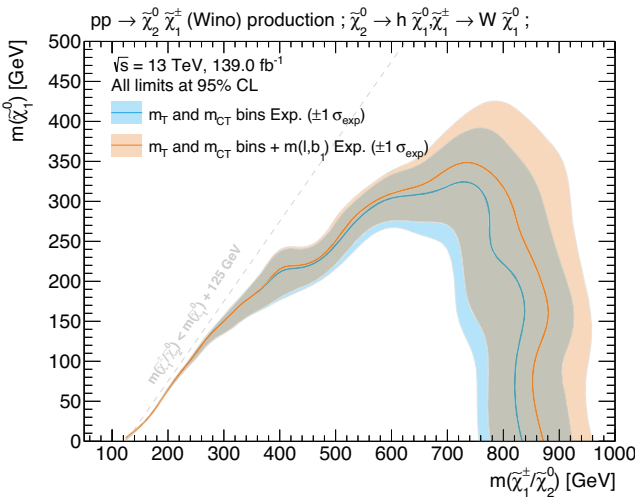


**Figure A.9:** Comparison of different shape-fit configurations, illustrating the sensitivity increase achieved through a requirement on high  $m_{\ell b_1}$  values in SR-HM on top of the two-dimensional shape-fit in  $m_T$  and  $m_{CT}$ . All exclusion limits shown are expected limits at 95% CL, using MC statistical and 30% systematic uncertainties. Background estimation in the signal regions is taken directly from MC for all SM backgrounds.

### A.3 Background estimation

The signal contamination in all validation regions is shown in fig. A.10. In the VR-off regions the maximum signal contamination is found to be about 7%–13%, depending on the requirement on  $m_T$ . In the VR-on regions, the maximum signal contamination amounts to about 5%–14%, depending again on the  $m_T$ -bin.

### A.4 Summary of results of ATLAS searches for SUSY

Figure A.11 provides a comprehensive summary of current results of ATLAS searches for SUSY. The limits on the sparticle masses set by different searches in various models and signatures are given.

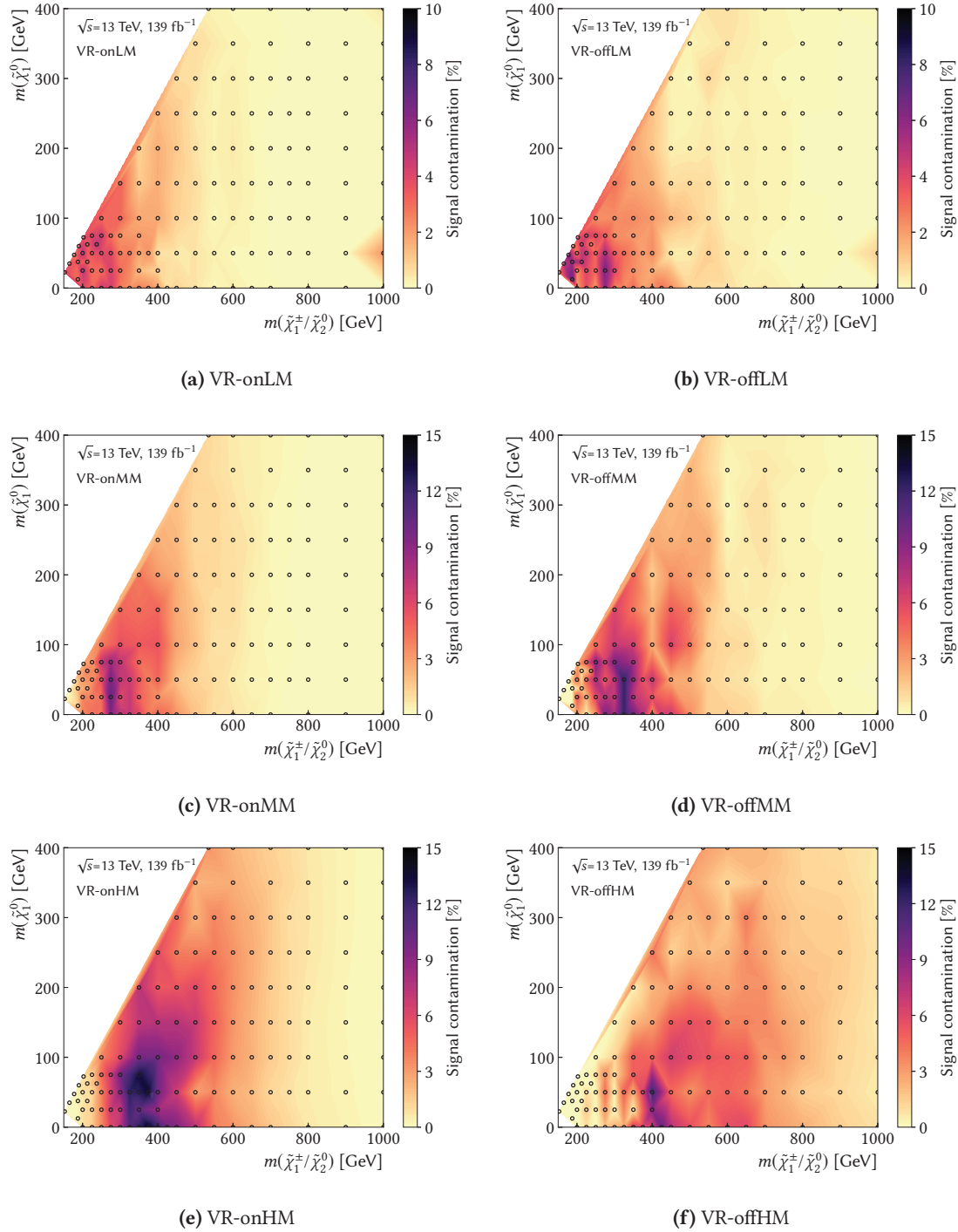


**Figure A.10:** Signal contamination (shown on the  $z$ -axis) for all VRs throughout the signal grid. The space between the signal points (indicated by the black circles) is interpolated using Delaunay triangles.











## B.2 Simplified likelihood results

Figures B.4 and B.5 highlight the limitations of the simplified likelihood approach using the ATLAS compressed and stop searches, discussed in section 10.5.

Figures B.6 and B.7 directly compare the expected and observed  $\text{CL}_s$  values obtained using both likelihood configurations for each ATLAS SUSY search considered. Both linear- and log-scale representations are shown, revealing that the simplified likelihood tends to lead to good agreement in the  $\text{CL}_s$  values around 0.05, while slightly overestimating sensitivity in the region with  $\text{CL}_s \ll 0.05$ , where signal models are in any case being excluded.

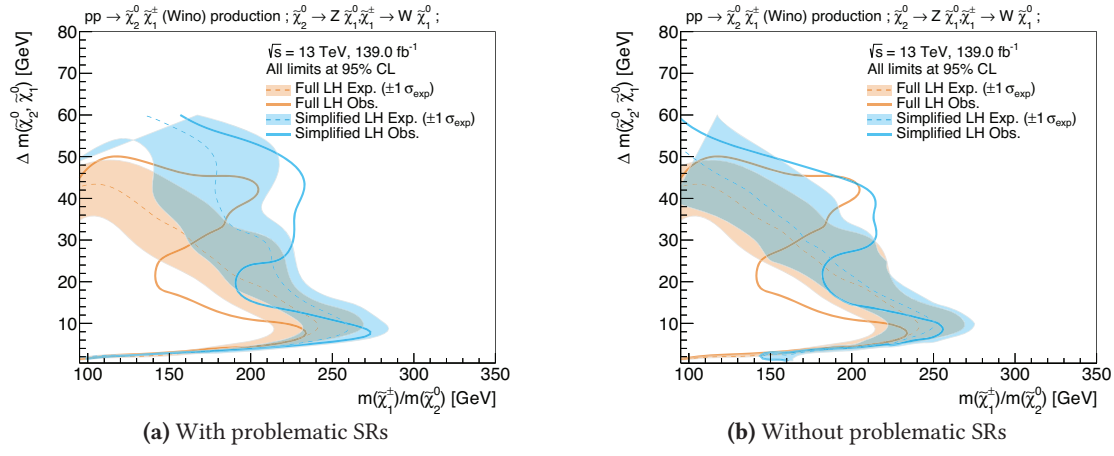


**Figure B.4:** The contours obtained with the full and simplified likelihoods of the ATLAS compressed search [91] are shown with the problematic signal regions (a) included in the simplified likelihood and (b) removed from it. A noticeable improvement in agreement between the two likelihoods is observed after removing the signal regions responsible for the instabilities discussed in section 10.5.

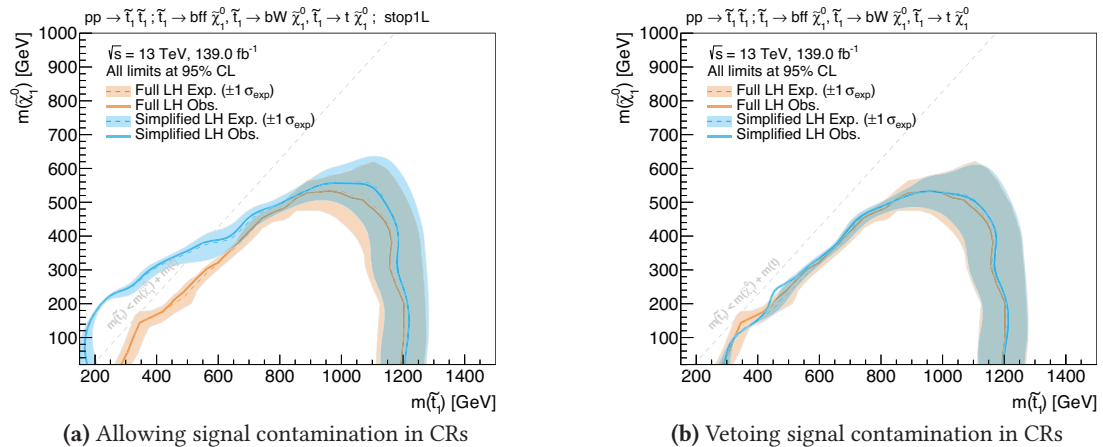


**Figure B.5:** Contours obtained with the full and simplified likelihoods of the ATLAS stop search. In fig. (a) the simplified likelihood is also applied on signal points with  $m(\tilde{t}_1) < m(\tilde{\chi}_1^0) + m(t)$ , where significant signal contamination in the CRs occurs. In fig. (b), such signal points are removed and thus not evaluated using the simplified likelihood.

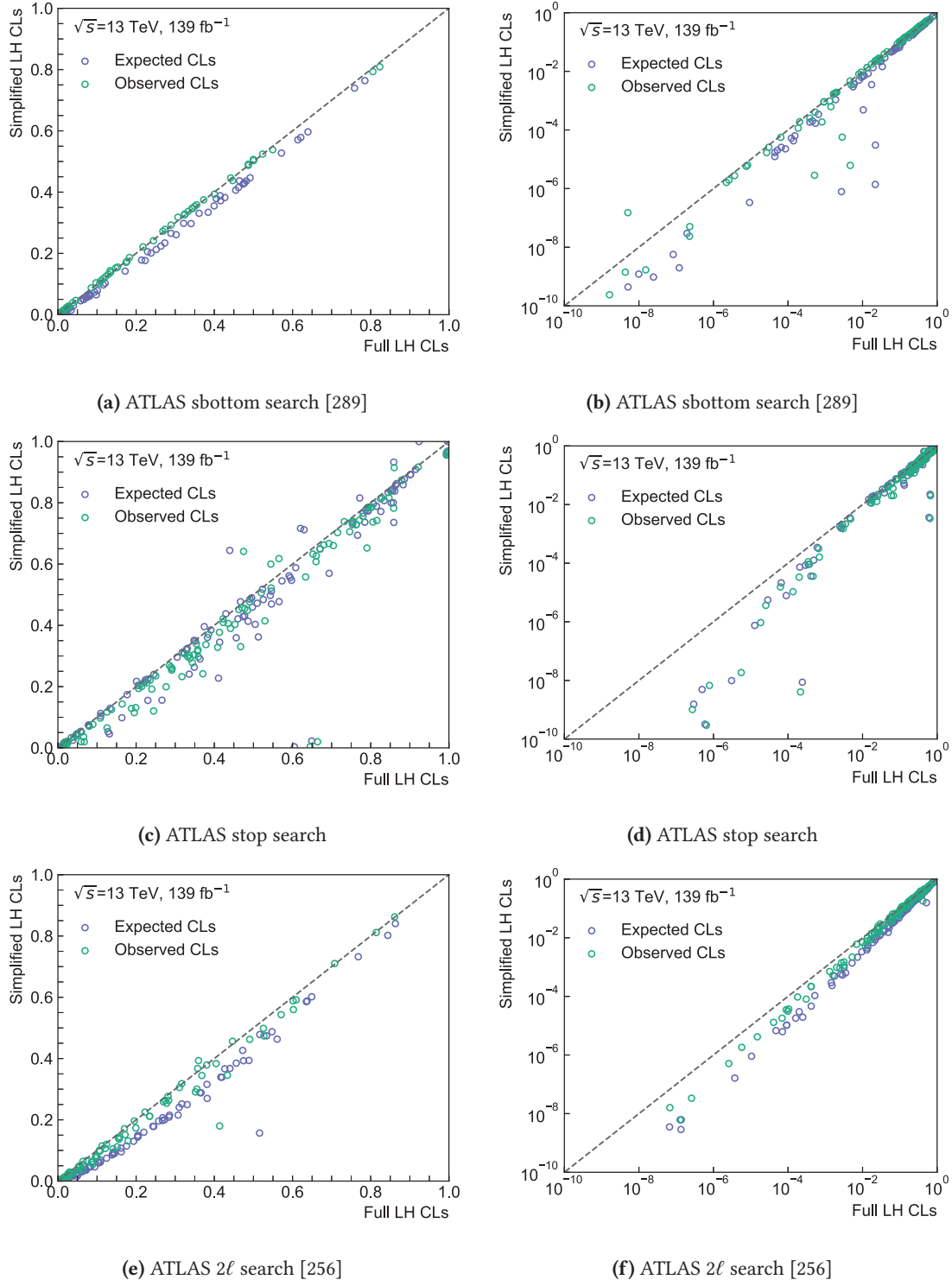


**Figure B.6:** Scatter plots comparing the observed and expected  $\text{CL}_s$  values obtained using the simplified and the full likelihoods for the same set of signal models originally considered in the various ATLAS SUSY searches. Both linear and logarithmic scale representations are shown on the left- and right-hand side, respectively, illustrating the full range of  $\text{CL}_s$  values. Apart from the scales, the left-hand and right-hand plots in each row do not differ from each other.

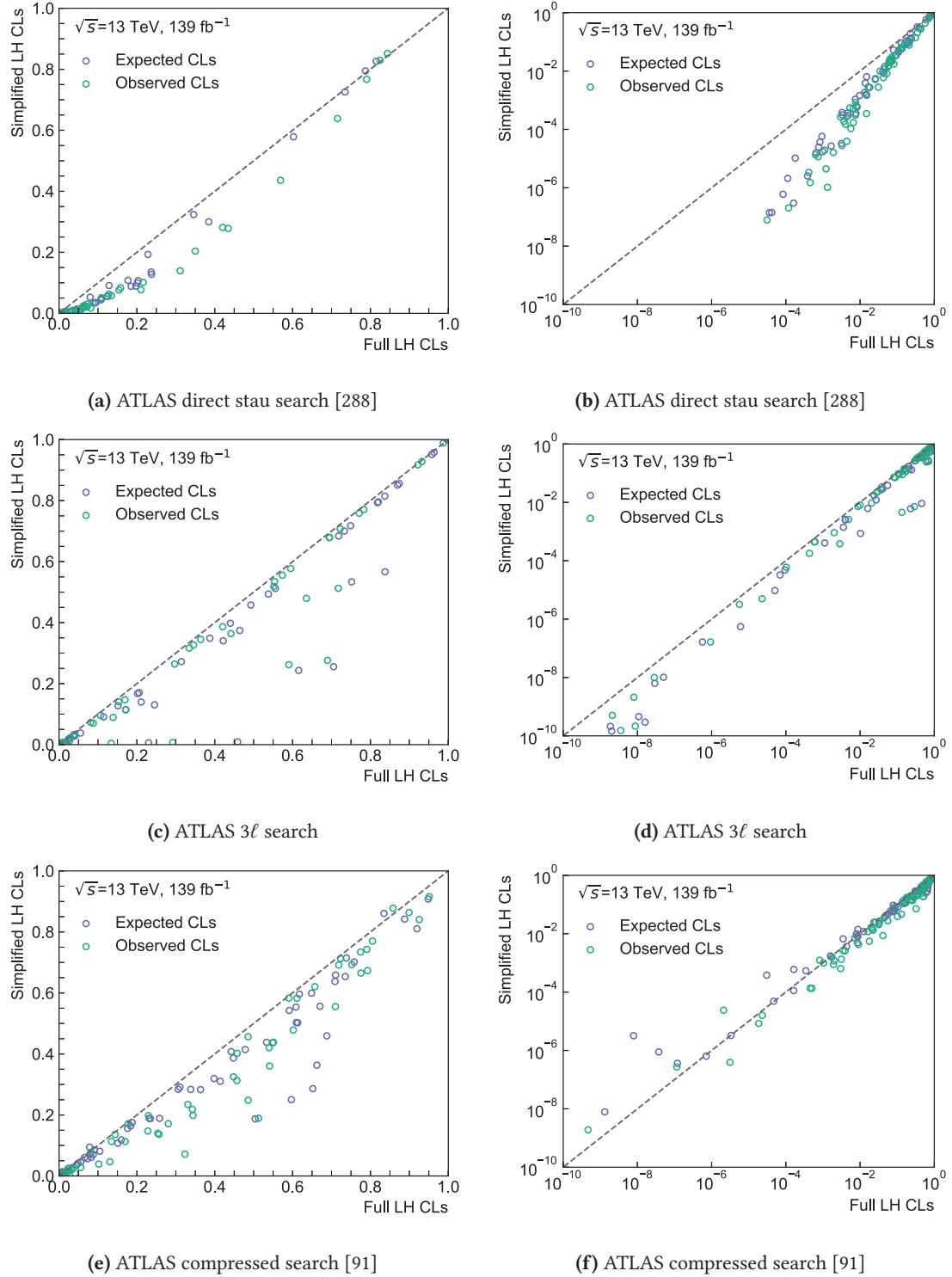


**Figure B.7:** Scatter plots comparing the observed and expected  $\text{CL}_s$  values obtained using the simplified and the full likelihoods for the same set of signal models originally considered in the various ATLAS SUSY searches. Both linear and logarithmic scale representations are shown on the left- and right-hand side, respectively, illustrating the full range of  $\text{CL}_s$  values. Apart from the scales, the left-hand and right-hand plots in each row do not differ from each other.





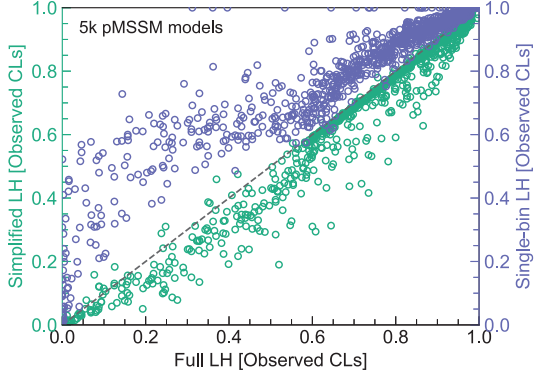


**Figure C.1:** Observed  $\text{CL}_s$  values obtained for all pMSSM models sampled for different likelihood configurations of the  $1\ell$  search. In green, the simplified likelihood discussed in chapter 10 is compared with the full analysis likelihood. In purple, the single-bin likelihood configuration using the discovery signal regions is compared with the full likelihood.

## C.2 Phenomenology of the LSP

Figure C.2 shows the LSP type as a function of the pMSSM parameters  $M_1$ ,  $M_2$ ,  $\mu$  and  $\tan \beta$ . Models with  $|M_1| \ll |M_2|, |\mu|$  tend to have an LSP with dominant bino component, while models with  $|M_2| \ll |M_1|, |\mu|$ , have an LSP that is mostly wino-like. Similarly, models with  $|\mu| \ll |M_1|, |M_2|$  have mostly higgsino-like LSPs. The parameter  $\tan \beta$  does not have a large impact on the LSP type within the ranges sampled.

Figure C.3 shows the fraction of models excluded by the  $1\ell$  search in different two-dimensional projections on the electroweakino masses. Models with a bino-like LSP tend to have nearly mass-degenerate  $\tilde{\chi}_1^\pm$  and  $\tilde{\chi}_2^0$  and are thus close to the canonical simplified model considered in the search. Models with a wino-like LSP have nearly mass-degenerate  $\tilde{\chi}_1^\pm$  and  $\tilde{\chi}_1^0$ . In such models, the  $1\ell$  search can be sensitive to  $\tilde{\chi}_2^\pm \tilde{\chi}_2^0$  production.

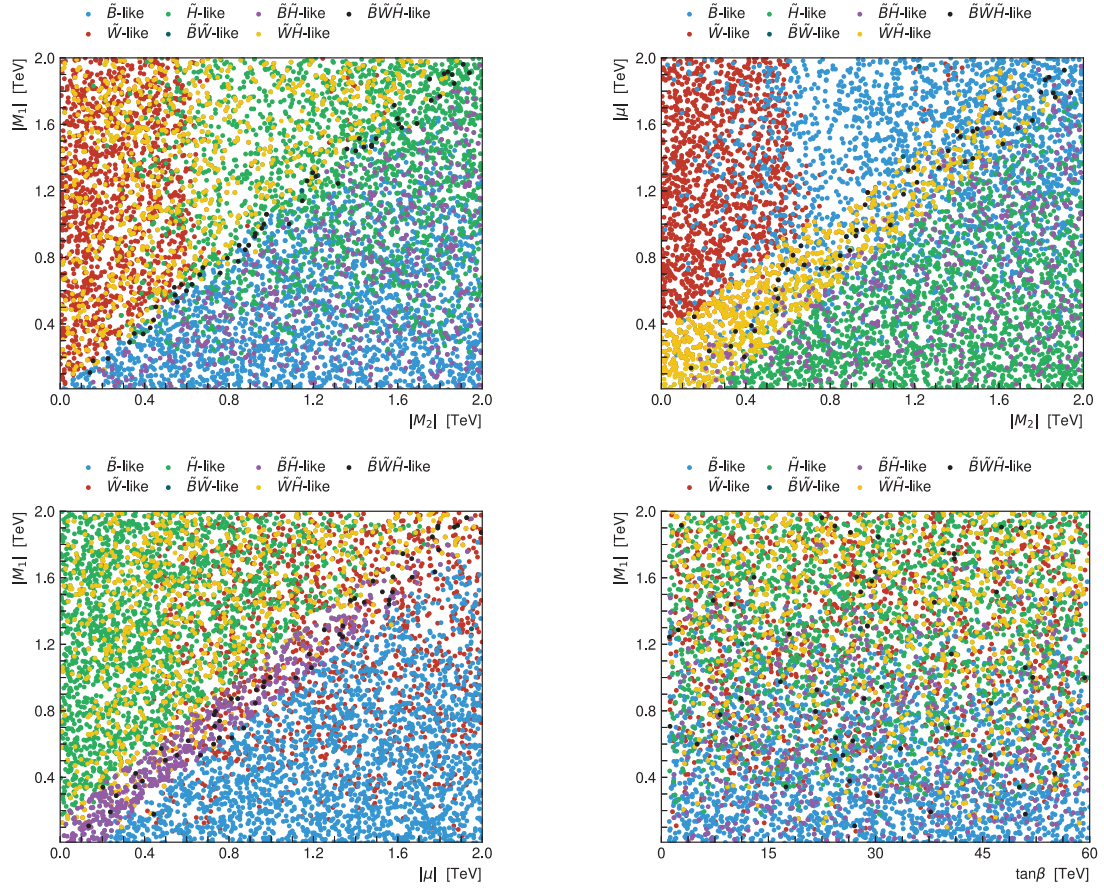


**Figure C.2:** Phenomenology of the LSP as a function of two-dimensional projections of the pMSSM parameter space. Each point in the plots corresponds to a unique pMSSM model sampled. The colour codes the nature of the LSP using the definitions introduced in section 11.3.



### C.3 Model properties

As illustrated in fig. C.4, the couplings of the  $\tilde{\chi}_2^0$  to the Higgs boson are suppressed by powers of  $|\mu|/M_2$  in the wino-like and bino-like scenarios [301], meaning that the branching fraction of  $\tilde{\chi}_2^0 \rightarrow h\tilde{\chi}_1^0$  takes on reasonably high values only in models with an LSP that is nearly pure bino.

Figure C.5 shows the compressed mass spectrum of an exemplary pMSSM model point with higgsino-like  $\tilde{\chi}_1^0$ , a model that the  $1\ell$  search is not expected to be sensitive to.

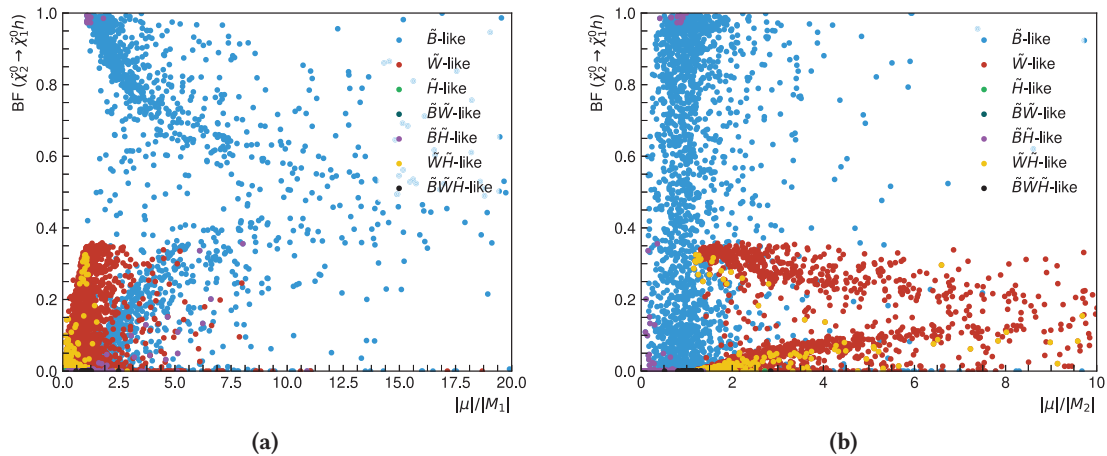


**Figure C.4:** Density of the pMSSM models projected onto the plane spanned by  $\text{BF}(\tilde{\chi}_2^0 \rightarrow h\tilde{\chi}_1^0)$  and (a)  $|\mu|/|M_1|$  or (b)  $|\mu|/|M_2|$ . Models are shown as a function of their  $\tilde{\chi}_1^0$  type.

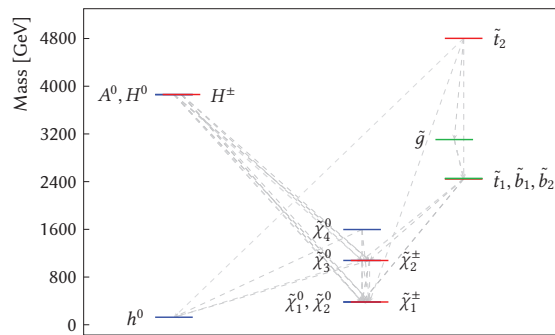


**Figure C.5:** Mass spectrum of an exemplary pMSSM model with higgsino like lightest electroweakinos. The branching fractions of the different decays are indicated through the width and and greyscale colour (pure black being 100%, pure white being 0%) of the arrows. Branching fractions below 10% are suppressed for the sake of visibility. Figure generated using `pyslha` [92].

### C.4 Impact of the $1\ell$ search on the pMSSM parameters

In fig. C.6, the impact of the  $1\ell$  search on the remaining pMSSM parameters sampled, not already shown in section 11.4.2, are provided. As before, the full set of models evaluated with the  $1\ell$  search is shown as black line, while the bin-wise number of models excluded by the search are indicated with the blue histogram. An additional pad indicates the bin-wise fraction of models excluded.

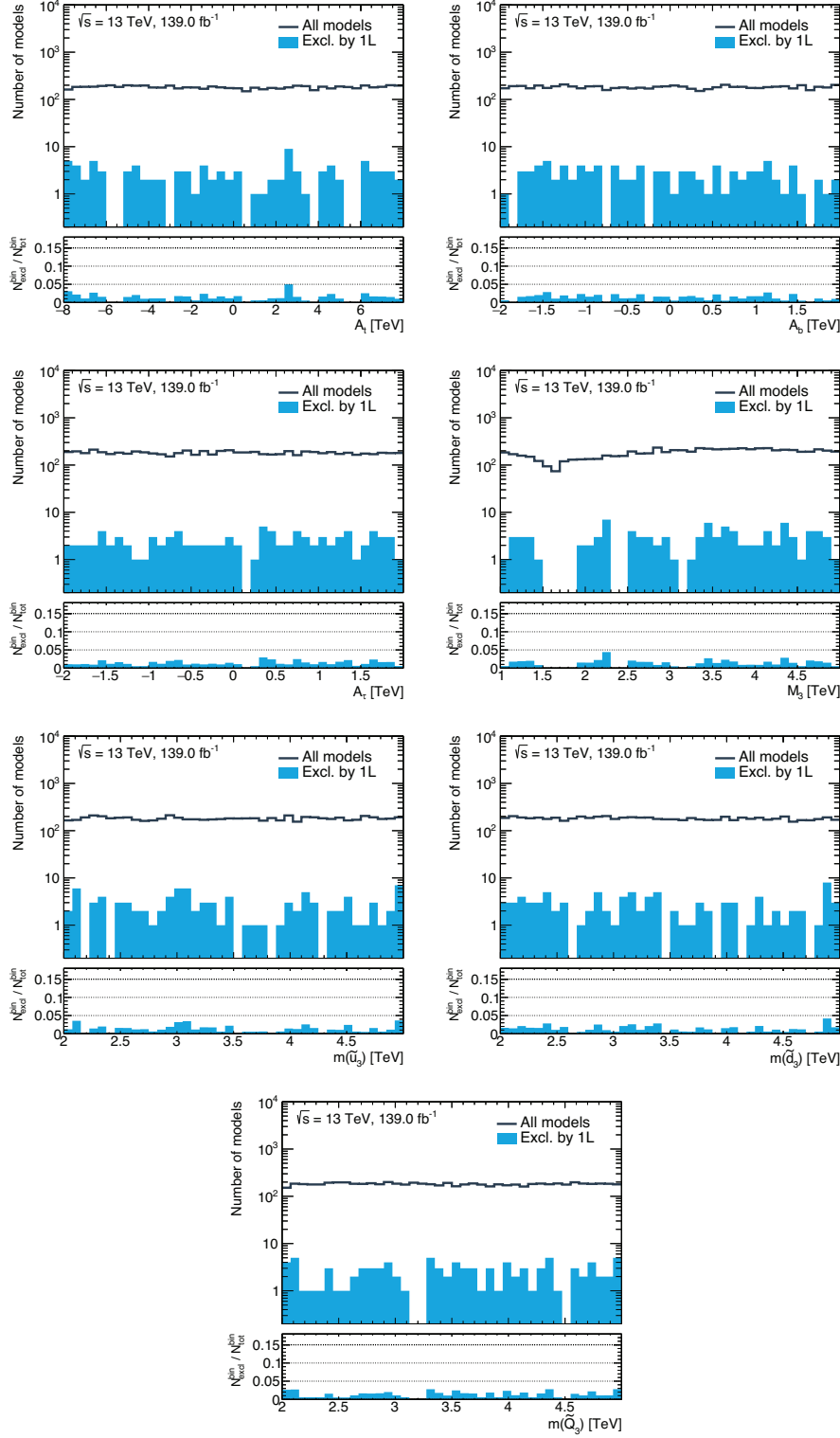


**Figure C.6:** Bin-by-bin number of excluded models as a one-dimensional function of the remaining pMSSM parameters not already shown in fig. 11.7. The bin-wise fraction of excluded models,  $N_{\text{excl}}^{\text{bin}} / N_{\text{tot}}^{\text{bin}}$ , is shown in the lower pad. All models are evaluated using the simplified likelihood of the 1 $\ell$  search.

## C.5 Impact of the $1\ell$ search on the dark matter relic density

Figure C.7 compares the density of pMSSM models in a two-dimensional projection on the  $\Omega_{\tilde{\chi}} h^2 - m(\tilde{\chi}_1^0)$  plane before and after the conservative LEP constraint on the chargino mass of  $m(\tilde{\chi}_1^\pm) > 92 \text{ GeV}$  [90] is applied. Only models with a bino-like LSP provide a light LSP with mass below  $10^2 \text{ GeV}$  after the LEP constraint. In order for the  $Z$ - and  $h$ -funnels to become visible, i.e. for there to be a sizeable number of models with a light bino-like LSP and  $\Omega_{\tilde{\chi}} h^2 < 0.12$ , the region with  $m(\tilde{\chi}_1^0) < 10^2 \text{ GeV}$  would need to be oversampled. Due to the lack thereof within the scope of this thesis, only a small number of such models are sampled and subsequently evaluated using the  $1\ell$  search.

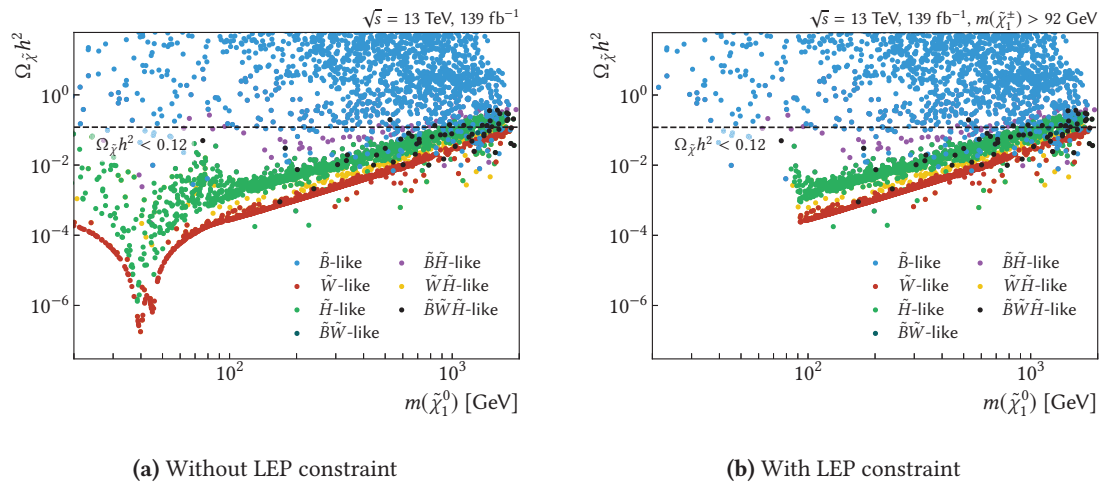


**Figure C.7:** Density of the pMSSM model points sampled in the plane spanned by the relic density and the  $\tilde{\chi}_1^0$  mass. The model points are additionally shown as a function of the nature of their  $\tilde{\chi}_1^0$ . In fig. (a) all pMSSM models originally sampled and evaluated are shown. In fig. (b), only models satisfying the constraint  $m(\tilde{\chi}_1^\pm) > 92 \text{ GeV}$  set by LEP [90] are shown. The horizontal dashed line represents the DM relic density measurement by the Planck Collaboration, interpreted as an upper limit such that the  $\tilde{\chi}_1^0$  can be a sub-dominant DM component.

















































